Model test of a hydroelastic truncated floating bridge with a stay-cable tower

Thomas Viuff [a],[*], Senthuran Ravinthrakumar [a], Ole David Økland [a], Ole Anton Grytå [b], Xu Xiang [b]

[a] *SINTEF Ocean AS, Trondheim, N-7465, Norway*
[b] *Norwegian Public Roads Administration (NPRA), Oslo, N-0667, Norway*

ARTICLE INFO

ABSTRACT

Experimental studies of long offshore and coastal structures such as very long floating bridges are challenged by the combination of coastal wave environments with relatively small design waves and excessive structural dimensions. It is often not possible to fit the entire model into the limited available space while at the same time being able to properly model the incoming waves. The sensible choice when deciding between such opposing model scale requirements, is to allow for a proper physical representation of the wave environment while finding alternatives to circumvent the space limitations. One way to do this is by truncating the original model design at carefully selected locations along the bridge and inserting passive or active boundary conditions so as to maintain similar static and dynamic properties as the prototype. The present study gives an in-depth description of the as-build experimental model of a truncated section of the Bjørnafjord phase 5 K12 concept, with simplified passive boundary conditions. The truncated section includes a complex double-curved geometry of the bridge girder connecting a cable-stayed tower at the southern end with ten floating pontoons at the northern end. The truncation points coincide with the tower column and the first moored pontoon of the full bridge. The boundary conditions in the bridge girder at the truncation points are simplified as fixed while allowing for free rotation around the vertical and longitudinal axes at the end with the otherwise moored pontoon. The truncated model is extensively instrumented in order to capture three degrees of freedom (DOF) motions at 13 locations along the bridge girder as well as six DOF motions of each pontoon. Force transducers capture the bridge girder and stay-cable axial forces, while strain gauges measure shear forces, bending moments and torque at 12 locations along the bridge girder and at each pontoon column.

The present study aims at documenting fundamental properties of the as-build model in order to act as a base for future verification and calibration of design tools used for similar floating bridge concepts. This encompasses a detailed description of the complex geometry, mass and stiffness properties of the structural parts and important responses from static documentation tests. Natural periods and corresponding modal response of the first two structural modes are captured from a horizontal decay test and finally the responses from pure current tests are discussed. The present study is focused on documenting the as-build experimental model while a separate paper is to be published later on focusing on results from tests with combinations of waves and current.

1. Introduction

In the previous decades, research in Norway has been advancing the understanding and modelling of floating bridges with the aim of improving the country's infrastructure. The aim is to establish fixed links over the many deep and wide fjords along the west coast. Floating bridges have been used extensively as temporary structures for crossing stretches of water for various purposes throughout history and one of the first permanent floating bridge structures in modern times was build around 1940 in the United States (see for instance Viuff (2020) and Moan and Eidem (2020) for brief historic overviews of past developments within the field). Later on, extensive scientific studies on

floating bridges were carried out in the early 1970s in both the United States and Norway and since then the idea of utilizing such structures as a reliable option for crossing deep and wide bodies of water has continuously matured into many permanent floating bridge structures around the world today. From the advancements within floating bridge structural dynamics, three notable bridge projects were constructed — the Hood Canal Bridge (1961) in the United States and the Bergsøysund Bridge (1992) and the Nordhordland Bridge (1994) in Norway, with the latter being conceptually similar to the one described in the present study. During the design of the two Norwegian bridge concepts, small scale experiments were performed in order to verify the design and the

calculation methods used, e.g. two-dimensional experiments of a rectangular pontoon with incoming regular waves referred to by Holand et al. (1977), three-dimensional hydro-elastic experiments of a single pontoon with different stiffnesses (Aarsnes et al., 1990) and of a generic curved floating bridge with eight discrete pontoons (Aarsnes et al., 1989). With the largest dimension of the floating bridge structure, described by Aarsnes et al. (1989), being less than 900 m in full scale it was possible to fit the entire structure inside the test facility using a model scale of 1:40. As the tests performed were based on Froude similarity, the wave environment could be properly modelled and the results have later been used for validation of calculation methods and software, see for instance Statens vegvesen (1990), Løken et al. (1990) and more recently (Xiang and Løken, 2019; Viuff et al., 2020b; Dai et al., 2022).

In recent years, extensive numerical studies have been conducted on floating bridge responses under various load conditions related to the many new concepts initiated over the years (Viuff, 2020; Moan and Eidem, 2020) and field measurements of the Bergsøysund Bridge have been compared to numerical predictions (Kvåle, 2017; Petersen et al., 2019). With the inherent uncertainties related to field measurements, simplified engineering assumptions and uncertainties generally related to numerical modelling (Viuff et al., 2020a), new experiments have been planned to further validate and calibrate the numerical models. The new test campaign includes both single- and multi-pontoon model tests as Xiang et al. (2018) have shown that multi-body hydrodynamic interaction effects influence the response of floating bridge structures with similar pontoon dimensions and distances between the pontoons. Fixed and forced motion tests were performed in 2017 by Baarholm (2017) for a single, elliptically shaped pontoon with and without an extending bottom plate to obtain excitation forces and added mass and damping coefficients for five degrees of freedom (DOFs) as well as estimating the effect of the extended bottom plate on the pontoon hydrodynamic performance. The experiments were later compared to viscous drag coefficients from the literature and simulations using Computational Fluid Dynamic (CFD) by Shao et al. (2019) in order to better understand the viscous drag loads and scale effects. It was shown that by incorporating Keulegan–Carpenter (KC) dependent drag loads, the CFD simulations fitted better to the experimental data. Ravinthrakumar et al. (2023a) published results from a recent test campaign related to the same Bjørnafjord phase 5 K12 floating bridge concept described in the present study. Their experimental models were made in scale 1:25 and the tests included: (i) single pontoon forced motion tests for the DOF related to the transverse motion of the floating bridge, (ii) single pontoon tests under various wave- and current conditions with fixed and flexible boundary conditions, and (iii) same tests as in (ii) but with two adjacent pontoons with fixed boundary conditions. In this way the multi-body hydrodynamic interaction effects were investigated for the most simple three-dimensional representation of the floating bridge.

In the last few years the LFCS (Design and Verification of Large Floating Coastal Structures) project (SINTEF Ocean, 2021a) has been mapping the current state of the art for both numerical- and experimental modelling related to large floating coastal structures, to give recommendations to design guidelines for the design of said structures and establish methods and tools for hydroelastic analysis of dynamic responses in inhomogeneous wave environments due to the unprecedented spatial dimensions. Included in the project was the development, description and finally conduction of a truncated model test of a long, straight, side anchored floating bridge concept for the Bjørnafjord crossing. Rodrigues et al. (2020) provides a presentation of the project and a summary of the related review work (Fergestad et al., 2018; Fonseca and Bachynski, 2018; Leira et al., 2018; Abrahamsen and Stansberg, 2019) for the development of the experimental test campaign for a truncated straight floating bridge concept with side mooring. The experimental model and test campaign is described in detail by Rodrigues et al. (2022) and many of the considerations related to the experimental campaign have been included in the development of the model test described in the present paper.

The present experimental study is meant as a reference for validation and calibration of design tools related to the wave- and current-induced structural response of the floating bridge concept or similar bridge concepts. Emphasis is put on the responses of the as-build truncated model with any comparison between the as-build model and the prototype being outside the scope of the present study. During design of the truncated model, a non-linear, coupled hydroelastic finite element model was produced in SIMA (SINTEF Ocean, 2021c,b) (a non-linear aero-hydro-elastic finite element program allowing for large displacements, generally used for offshore slender structures) to evaluate design choices prior to the model construction and for quality assurance (QA) during documentation tests prior to the wave- and current tests in the Ocean Basin. Note that any numerical results given in the present paper refer to the numerical model of the as-build, truncated floating bridge model.

The paper is organized in the following way: Section 2 gives a detailed description of the as-build model geometry and structural properties, Section 3 gives an overview of the instrumentation along the entire bridge and Section 4 describes the full test program used. Finally, Sections 5 and 6 lists the findings and conclusions, respectively.

2. Experimental model description

The as-build model is based on a design specification document (Xiang and Løken, 2020) formulated by the Norwegian Public Roads Administration (NPRA) and is a simplification of the full Bjørnafjorden phase-5 K12 concept report (AMC, 2019). The full floating bridge design is 5530 m long and has a total of 38 pontoons, of which three are moored to the seabed, cf. Fig. 1. The experimental model is a 1630 m long truncated section of the full floating bridge. The truncated section starts from the tower with a reduced number of cables, selected according to an *equivalent cable concept* for simplicity, and transitions into the floating bridge section until, but not including, Pontoon-11. Based on preliminary numerical studies, the static and dynamic properties of the truncated stay-cable tower remains similar to the full bridge model. The bridge girder above Pontoon-11 is a natural boundary condition for the truncated bridge model, since it is the first along the bridge to be moored to the seabed, as illustrated in Fig. 1. The truncated section is in the following referred to as the floating bridge or the model.
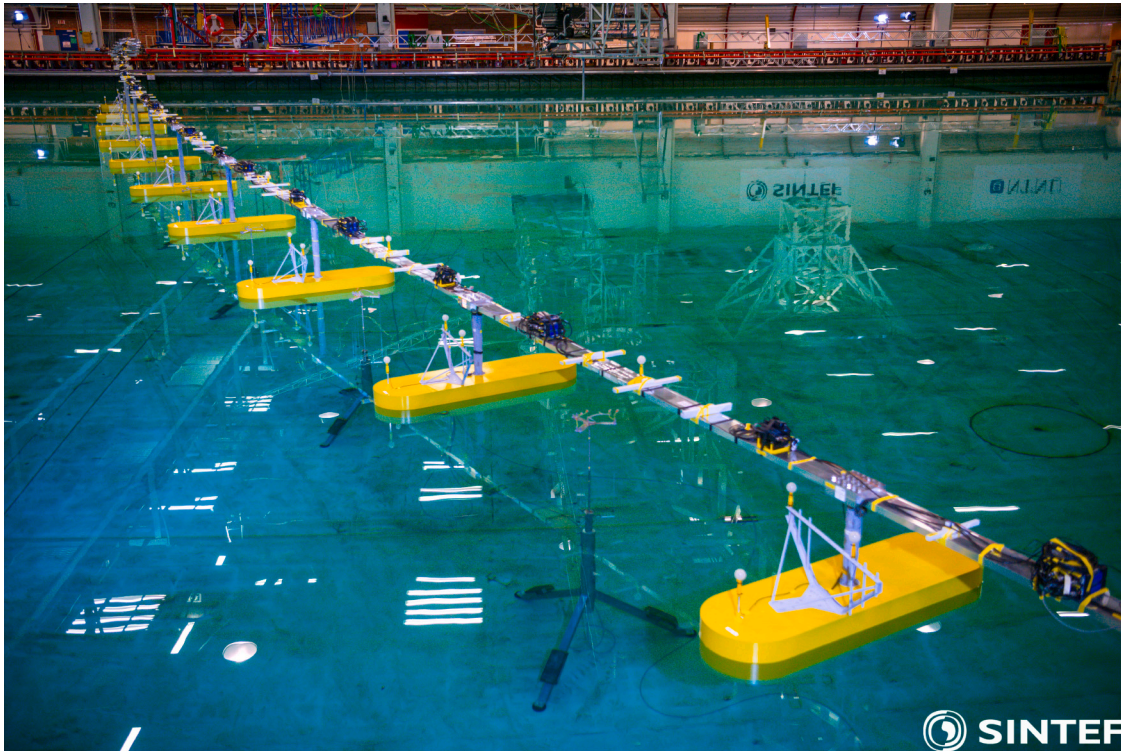
The as-build model in the Ocean Basin is sketched in Fig. 2 with corresponding nomenclature and relevant coordinate systems. It consists of a single *A*-shaped tower at the southern end connected to the horizontal bridge girder with 5×2 pre-tensioned stay-cables. This section is referred to as the cable-stayed bridge section or the main span. Following this section is the floating bridge section, where the bridge girder is resting on columns of various lengths connected to ten identically shaped floating pontoons. These individual model elements are joined by various clamped, rigid body connections. Finally, the floating bridge model is held in place by specified boundary conditions at the bridge girder ends and at the upper ends of each stay-cable. In the following sections, each individual part of the model is described in more details.

2.1. Model scale, water depth and orientation in the Ocean basin

The model tests were carried out in the Ocean Basin at SINTEF Ocean. The Ocean Basin has the outer dimensions $50 \times 80 \times 10$ m with an adjustable floor and two wavemakers (WM2 and WM3) with corresponding beaches on opposing sides, cf. Fig. 3. Current and long-crested waves can be generated from the WM2 side and short-crested waves can be generated from WM3. The model tests are carried out such that the floating bridge model is subjected to incident waves from different *going towards* heading angles relative to the global coordinate
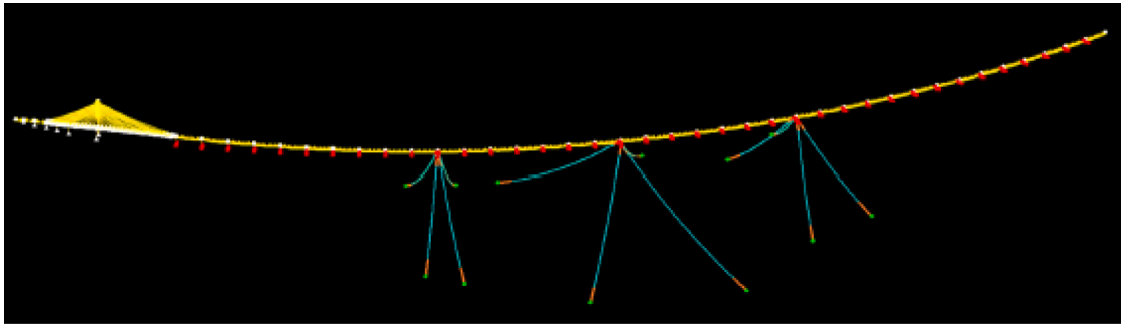
(a) Illustration of the full Bjørnafjord floating bridge phase-5 K12 concept (Xiang and Løken, 2020).

(b) Photo of the as-build model in the Ocean Basin in the Configuration A position with Pontoon-10 in the front and the stay-cable tower in the background.

Fig. 1. Illustrations of the prototype model and the as-build model of the truncated section.

system shown in Fig. 2. In order to achieve all the different incident heading angles, the model tests have been performed for three different configurations of the floating bridge in the Ocean Basin:

- Configuration A: Incident headings of 220° (WM2 waves and current) and 310° (WM3 waves only)
- Configuration B: Incident headings of 85° (WM2 waves and current) and 175° (WM3 waves only)
- Configuration C: Incident headings of 130° (WM2 waves and current) and 220° (WM3 waves only)

For each configuration, the floating bridge model has been (re-)assembled and the pre-tension in the stay-cables have been tuned according to target values as well as a target idealized floating bridge geometry.

All model properties are converted from model scale to full scale by applying Froude's scale law with a model scale of 1:31. In addition, the mass properties and force measurements are multiplied by a factor of 1.025 to account for the fact that the model tests are carried out in fresh water, while the prototype is exposed to salt water. The water depth is set to 2.5 m (model scale) due to the need for strong current

velocities. The chosen depth corresponds to 77.5 m in full scale and falls within the conditions for deep water waves. Unless otherwise specified, all results refer to full scale.

2.2. Coordinate systems

In order to fully describe the complex geometry of the floating bridge model, various coordinate systems are introduced. These are a global $OXYZ$ coordinate system as well as various local $oxyz$ coordinate systems for the bridge girder, columns and pontoons, and the cables at the main span.

The right-handed, global $OXYZ$ coordinate system is used to describe the environmental conditions and the location of the pontoons, girders and other bridge components. The global coordinate system and the general orientation of the floating bridge is illustrated in Fig. 2. The positive Z-axis is defined as up and $Z = 0$ is at the still water level (SWL). The positive X-axis and Y-axis point towards North and West, respectively. The current- and wave direction are defined by the angle from the positive X-axis to the *going towards* direction of the respectable environments using the right-hand rule.
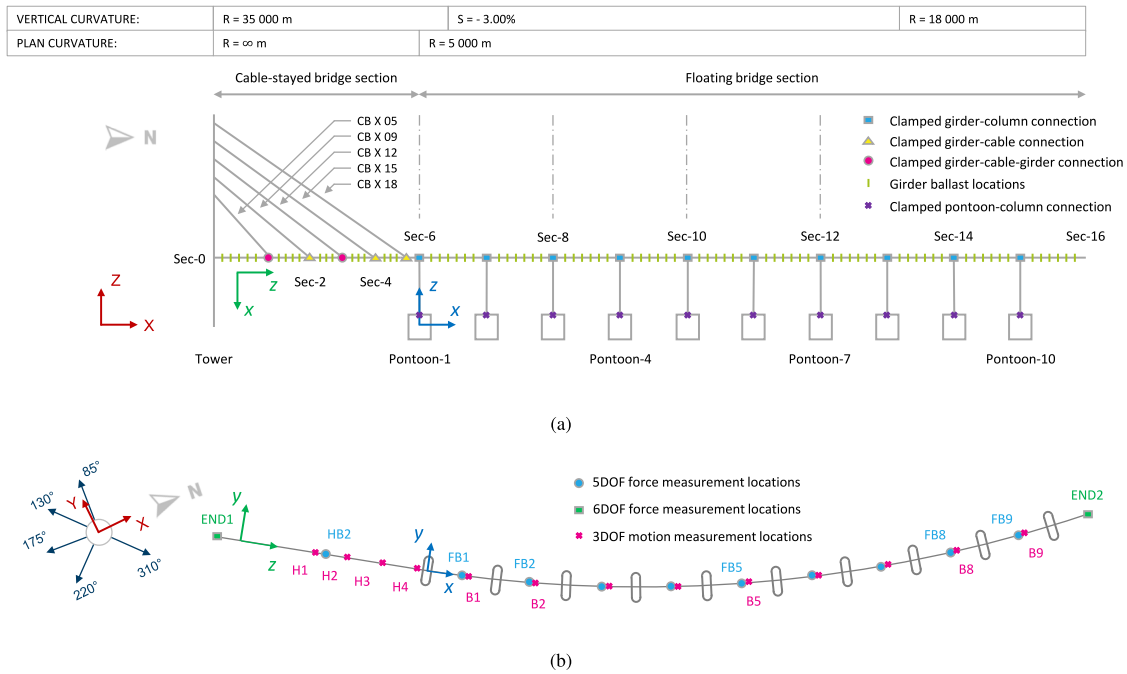
Fig. 2. Diagram of floating bridge model with relevant nomenclature and coordinate systems. (a) View from East, perpendicular to the roadline. The 'X' in the stay-cable name convention refer to EAST and WEST for stay-cables on either side of the bridge girder. (b) View from above. Measurements at the bridge girder are indicated along the bridge, as well as *going towards* wave directions of the performed wave tests.
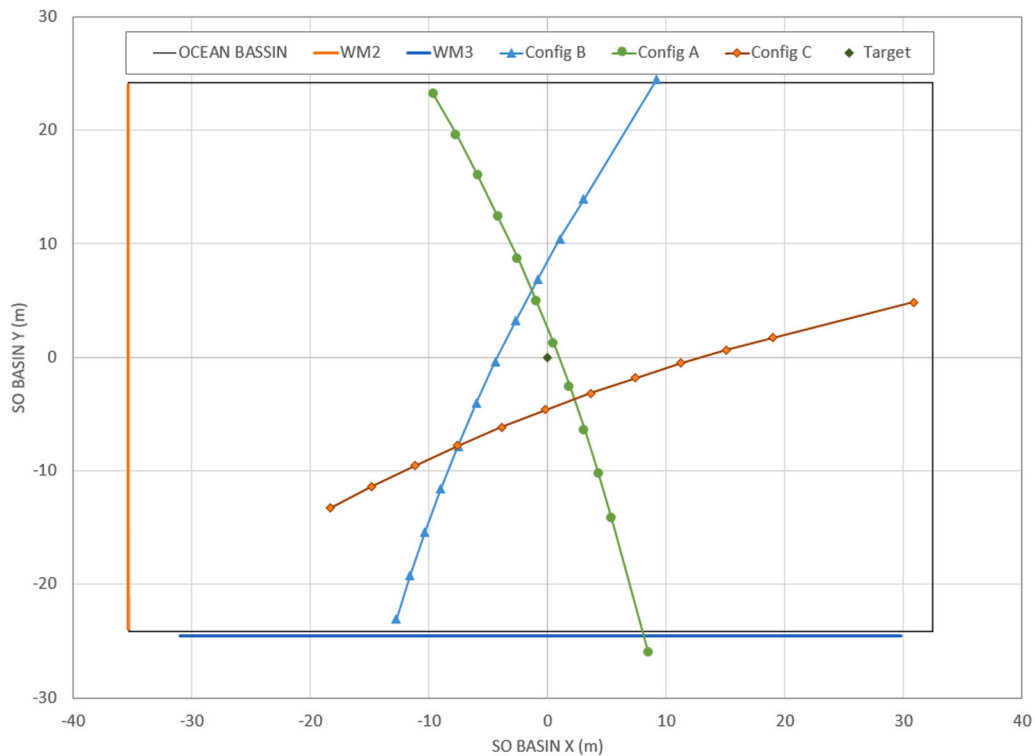
Fig. 3. Floating bridge configurations in Ocean Basin. The centre of the Ocean Basin is indicated by the target location.

The right-handed, local pontoon $oxyz$ coordinate systems are, for each pontoon, defined such that the origin is located at the geometric centre of the relevant pontoon at the SWL with the y-axis pointing in the pontoon longitudinal direction towards West, while the x- and z-axis are pointing in the pontoon transverse direction and upwards, respectively. These pontoon coordinate systems are also used to describe the column cross-sectional properties and measured responses.

The centreline of the pontoon columns follow the local z-axis of the pontoons.

A series of control sections along the bridge girder are listed in Section 2.3 to assist description of the idealized bridge girder geometry. The local, right-handed coordinate system $oxyz_k$ is used to define the k_{th} bridge girder cross-section properties, the orientation of the k_{th} control section (cf. Fig. 2 and Table 1), the relative positions of the

Table 1
Girder topology with X, Y and Z coordinates in global coordinates and azimuth and declination angles of the local bridge girder coordinate system.

Section	X (m)	Y (m)	Z (m)	Azimuth (deg)	Declination (deg)
Sec-0	489.81	−178.91	59.87	−35.28	91.01
Sec-1	571.44	−236.67	57.96	−35.28	91.18
Sec-2	636.75	−282.87	56.22	−35.28	91.31
Sec-3	685.73	−317.53	54.80	−35.28	91.41
Sec-4	734.71	−352.18	53.27	−35.28	91.51
Sec-5	783.69	−386.84	51.64	−35.28	91.60
Sec-6	800.02	−398.39	51.08	−35.28	91.64
Sec-6-7-transition	840.75	−426.90	49.62	−34.71	91.72
Sec-7	902.96	−469.30	47.36	−33.85	91.72
Sec-8	1007.63	−537.62	43.61	−32.42	91.72
Sec-9	1113.99	−603.31	39.86	−30.98	91.72
Sec-10	1221.95	−666.31	36.11	−29.55	91.72
Sec-11	1331.45	−726.59	32.36	−28.12	91.72
Sec-12	1442.43	−784.12	28.61	−26.69	91.72
Sec-13	1554.80	−838.86	24.86	−25.25	91.72
Sec-13-14-transition	1577.75	−849.61	24.10	−24.96	91.72
Sec-14	1668.52	−890.77	21.39	−23.82	91.40
Sec-15	1783.49	−939.82	18.76	−22.39	91.00
Sec-16	1899.65	−985.98	17.01	−20.96	90.60

cable connection points and the bridge girder boundary conditions. The origin of the bridge girder $oxyz_k$ coordinate system follows the continuous curve, i.e. roadline, from the end at the tower to the floating bridge section end. The local bridge girder coordinate system utilizes the right-hand-rule and is oriented with the local z_k-axis tangential to the bridge girder at all times. Correspondingly, the local y_k-axis is at all locations perpendicular to the bridge girder. Positive axis directions are illustrated in Fig. 2. The orientation of the k_{th} control section is based on an initial local coordinate system aligned with the global coordinate system. This initial local coordinate system is then first rotated by the listed azimuth angle around the local z_k-axis resulting in an intermediate coordinate system configuration. This intermediate configuration is then rotated by the listed declination angle around the intermediate y_k-axis. The resulting configuration is the one used for description of motion, forces and moments in the bridge girder.

2.3. Bridge girder

The bridge girder follows the geometry outlined with the vertical- and plane curvatures along the bridge, illustrated in Fig. 2. The azimuth and declination angles of the local bridge girder coordinate system described in Section 2.2 are used to describe the curvature along the roadline. A list of control sections is given in Table 1 and the notations are explained in Fig. 2. The control sections Sec-6-7-transition and Sec-13-14-transition indicate the two curvature transition points where the constant vertical slope of the bridge girder intersect tangentially with the vertical radii. In the following, the control sections Sec-0 and Sec-16 are also referred to as END1 and END2, respectively.

When designing the bridge girder, focus is placed on bending- and torsional stiffness properties, geometric accuracy, weight properties, stiff connections to stay-cables and columns, functionality during testing and robustness of strain gauge measurements. For this reason, it is important that the final, as-build stiffness- and mass properties are kept in mind. This implies that weight from amplifiers, power supplies, signal cables and so on must be considered when designing the bridge girder cross-section. A drawback of focusing on the bending- and torsional stiffness properties is that the axial stiffness of the bridge girder increases with a factor of roughly 30. In order to account for this change in the bridge girder axial stiffness, an axial spring is attached to the boundary condition at Sec-16. The spring design is further described in Section 2.8.

The entire bridge girder consists of 13 shorter bridge girder components connected with rigid clamped connections to each other and

to columns and stay-cables. A description of the clamped connections is given in Section 2.7. All bridge girder components are produced in aluminium with a box-shaped cross-section with a recess at the top and bottom to obtain correct torsional stiffness. Additionally, each bridge girder component is produced with the specified curvature about the weak- and strong axis. This is achieved by milling each individual girder component from an aluminium bar with a slightly larger cross-section than the produced girder component.

The cross-sectional properties of the bridge girder are listed in Table 2. The stiffness properties along the bridge girder are increased at locations with rigid, clamped connections to columns and some of the stay-cables. For more information see Section 2.7.

The bridge girder mass- and inertia properties listed in Table 2 are given for the girder only without excess mass from distributed instrumentation and clamps of the final, as-build structure. For a comprehensive list of the distributed masses along the bridge girder, the reader is referred to Appendix A.

2.4. Columns

Along the floating bridge model there is one column for each pontoon. The length of each column varies due to the changing bridge girder elevation along the bridge roadline. The location of each pontoon column in the horizontal plane is coinciding with the respective connecting pontoon and bridge girder control sections. The coordinates for the upper and lower ends of each pontoons are listed in Table 3 with X, Y and Z values in the global coordinate system. The lower ends are attached to the centre of the pontoons at the freeboard height, while the upper ends are located 2 m directly below the bridge girder neutral axis in the global coordinate system.

The columns are designed as flexible by using hollow, cylindrical, high-precision steel tubes. A rigid transition to the pontoon and the bridge girder is achieved by a 15 mm (model scale) thick steel flange at each end of the columns, bolted to the pontoon core cylinder and bridge girder clamps. The column length is defined as the inner distance between these two flanges.

The design of the column cross-sectional dimensions focus on providing correct stiffness properties, as well as a robust signal for strain gauge measurements. A high precision steel tube is used as basis for the columns. The designed wall thickness of the columns is achieved by milling the outer diameter. Due to practical circumstances, two slightly different combination of outer and inner diameters (providing similar bending stiffness properties) are used. The column properties are listed in Table 2 and are based on estimated values calculated from information of the column dimensions, material and instrumentation mass. Measured properties only deviate slightly from the ones listed here. The length of each column varies but they have the same three strain gauge positions (bottom, middle and top), resulting in unique mass properties for each column.

2.5. Pontoons

To support the bridge girder along the bridge, ten geometrically identical pontoons are equidistantly distributed with 125 m in between. The location and orientation follow the plan curvature and azimuth of the bridge girder neutral axis and are listed in Table 3. The pontoon plan geometry has a *circtangular* shape, meaning that in the horizontal plane, the geometry is made up of a rectangle in the middle with a half circle on two opposing sides, see Fig. 1(b). The outer dimensions of pontoons are listed in Table 4.

The pontoon models are designed to behave as rigid bodies and focus is placed on geometric accuracy and weight. Typically models must fulfil both, as well as being functional for testing. This implies that the pontoons, in addition to be carrying instrumentation and mechanical features, also need to carry weight from amplifiers, power supplies, instrumentation for motion measurement and so on. It is therefore

Table 2

Girder and column cross-section properties following local coordinate system axes. Mass and radius of gyration of the bridge girder are given for the girder only and do not include mass from distributed instrumentation and clamps.

Model part	Mass (tonne/m)	RoG_z (m)	EA_{zz} (kN)	EI_{xx} (kN m^2)	EI_{yy} (kN m^2)	GJ_{zz} (kN m^2)
Girder	12.488	1.475	9.775×10^9	2.070×10^{10a}	6.950×10^{8a}	8.386×10^{8a}
Column-1	6.056	0.932	4.835×10^9	2.100×10^9	2.100×10^9	1.616×10^9
Column-2	6.072	0.932	4.835×10^9	2.100×10^9	2.100×10^9	1.616×10^9
Column-3	6.091	0.932	4.835×10^9	2.100×10^9	2.100×10^9	1.616×10^9
Column-4	6.401	0.932	5.073×10^9	2.150×10^9	2.150×10^9	1.654×10^9
Column-5	6.430	0.932	5.073×10^9	2.150×10^9	2.150×10^9	1.654×10^9
Column-6	6.466	0.932	5.073×10^9	2.150×10^9	2.150×10^9	1.654×10^9
Column-7	6.515	0.932	5.073×10^9	2.150×10^9	2.150×10^9	1.654×10^9
Column-8	6.583	0.932	5.073×10^9	2.150×10^9	2.150×10^9	1.654×10^9
Column-9	6.674	0.932	5.073×10^9	2.150×10^9	2.150×10^9	1.654×10^9
Column-10	6.774	0.932	5.073×10^9	2.150×10^9	2.150×10^9	1.654×10^9

[a] Measured values.

Table 3

Location and orientation of pontoon local coordinate systems and column ends in the global coordinate system. Column length is given as inner distance between the column flanges used to connect the column to the adjacent pontoon and bridge girder clamps.

Pontoon/ Column	Both X (m)	Y (m)	Column specific Z (lower) (m)	Z (upper) (m)	Length (m)	Pontoon specific Z (m)	Azimuth (deg)
Pt-Clm-1	800.02	−398.39	3.50	49.08	45.58	0.00	−35.28
Pt-Clm-2	902.96	−469.30	3.50	45.36	41.86	0.00	−33.85
Pt-Clm-3	1007.63	−537.62	3.50	41.61	38.11	0.00	−32.42
Pt-Clm-4	1113.99	−603.31	3.50	37.86	34.36	0.00	−30.98
Pt-Clm-5	1221.95	−666.31	3.50	34.11	30.61	0.00	−29.55
Pt-Clm-6	1331.45	−726.59	3.50	30.36	26.86	0.00	−28.12
Pt-Clm-7	1442.43	−784.12	3.50	26.61	23.11	0.00	−26.69
Pt-Clm-8	1554.80	−838.86	3.50	22.86	19.36	0.00	−25.25
Pt-Clm-9	1668.52	−890.77	3.50	19.39	15.89	0.00	−23.82
Pt-Clm-10	1783.49	−939.82	3.50	16.76	13.26	0.00	−22.39

Table 4

Outer dimensions of the *circtangular*-shaped pontoons.

Length (m)	Width (m)	Height (m)	Draft (m)
53.00	14.90	8.50	5.00

important that the overall mass properties and water resistance are in focus. To facilitate the rigid body behaviour of each pontoon, the interior is build as a composite structure of aluminium and divinycell, cf. Fig. 4. This composite structure consists of an aluminium core cylinder, bottom plate, top plate and vertical webs in the longitudinal and transverse direction, creating four compartments, each filled with divinycell. A 3 mm (model scale) aluminium shell is glued to the divinycell structure. The result is a stiff composite structure. After gluing on the outer aluminium shell, the pontoons are painted and control weighed. The final mass properties of the various pontoons are listed in Table 5 with centre of gravity and gyration radii found from cradle tests.

2.6. Tower stay-cables

The main span of the bridge girder is supported by tower stay-cables at Sec-1 to Sec-5 with two stay-cables on either side, connecting to the tower. The locations of the upper and lower ends of each stay-cable in the global coordinate system are listed in Table 6. The position of the lower ends are defined relative to the local bridge girder coordinate system as $x = 1$ m and $y = \pm 14$ m at each of the control sections.

Focus in the cable system design is placed on axial stiffness and mass properties. Each stay-cable consists of an axial spring at the upper end, connected with a snap hook to an eye bolt at the tower. The other end of the spring is connected via an eye bolt to a 6 mm (model scale) steel rod. This rod is connected to a shear force transducer at the lower end,

Table 5

Measured pontoon mass properties. All pontoons have a point mass from the rigid pontoon-column connection in addition to the listed mass properties. This added ballast has a mass of 50.7 tonne and is located in the geometric centre of the pontoon at $z = 3.118$ m in the local pontoon coordinate system. The added ballast is <u>not</u> included in the pontoon mass and radii of gyration values listed here.

Structural part	Mass (tonne)	Centre of gravity CoG$_x$ (m)	CoG$_y$ (m)	CoG$_z$ (m)	Radii of gyration RoG$_x$ (m)	RoG$_y$ (m)	RoG$_z$ (m)
Pontoon-1	2243.59	0.000	0.221	−2.873	12.941	4.930	13.296
Pontoon-2	857.35	0.000	0.360	−1.447	15.533	5.570	15.601
Pontoon-3	1139.41	0.000	−0.304	−1.419	15.138	5.501	15.240
Pontoon-4	1102.22	0.000	−0.300	−1.218	15.465	5.491	15.578
Pontoon-5	1157.55	0.000	−0.310	−1.351	15.228	5.494	15.364
Pontoon-6	1183.93	0.035	−0.217	−1.504	15.045	5.542	15.142
Pontoon-7	1221.13	0.000	−0.284	−1.655	15.234	5.525	15.362
Pontoon-8	1250.78	0.000	−0.256	−1.812	15.039	5.550	15.159
Pontoon-9	1286.78	0.000	−0.268	−1.799	15.003	5.504	15.147
Pontoon-10	1307.08	0.000	−0.022	−1.866	15.037	5.508	15.181

which in turn is mounted on a transverse aluminium girder with custom shaped ends with an angle perpendicular to the axial direction of each cable, cf. Fig. 5(b). The transverse aluminium girder is connected to the bridge girder via rigid clamped connections, see Section 2.7. A nut is used to connect the lower end of the cable to the shear force transducer in order to adjust the pre-tension force during installation of the floating bridge.

An estimate of the stay-cable mass can be achieved from the length given in Table 6 and the mass density of the steel rod only, neglecting the excess mass of the spring at the upper ends due to the low inertia contributions to both static and dynamic properties of the bridge girder. The estimated mass properties are listed in Table 7.

The measured axial stiffness of each stay-cable set is listed in Table 7 together with the measured pre-tension values for each of the three
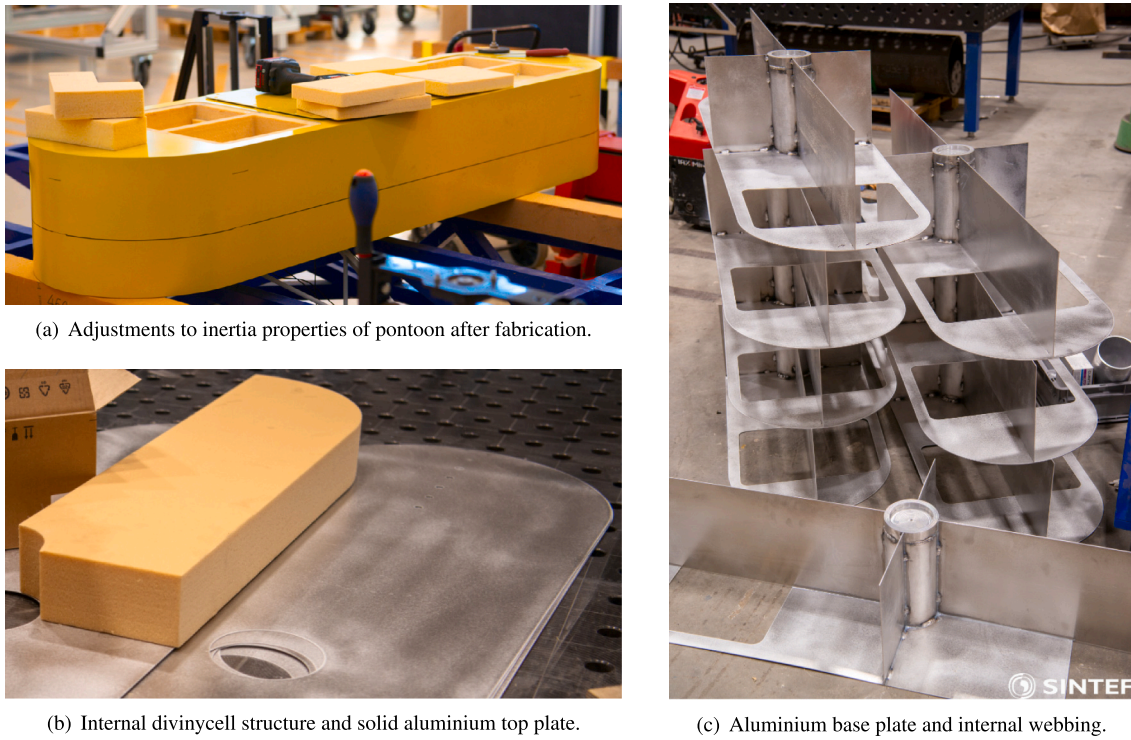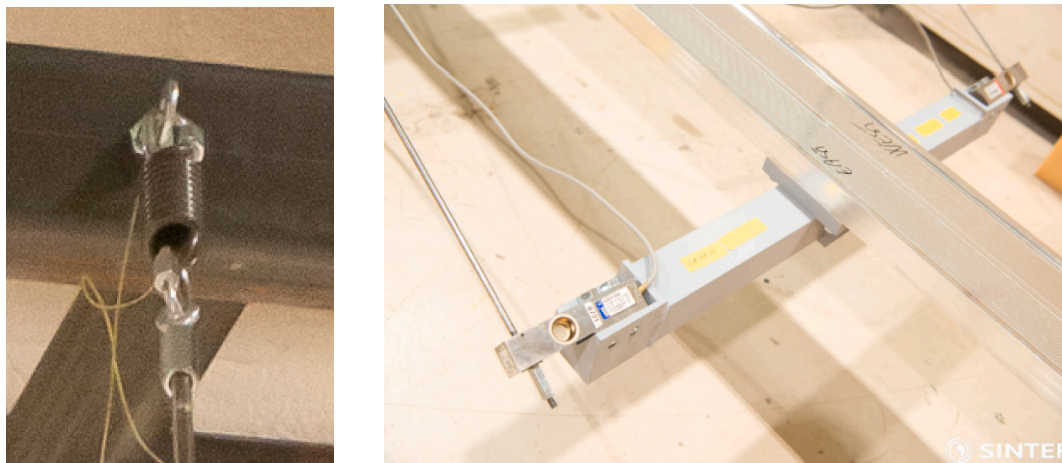
(a) Adjustments to inertia properties of pontoon after fabrication.

(b) Internal divinycell structure and solid aluminium top plate.

(c) Aluminium base plate and internal webbing.

Fig. 4. Photos taken of pontoons during fabrication.

(a) Axial spring at upper end.

(b) Connection to transverse girder and force transducer at lower end.

Fig. 5. Photos of tower stay-cable assembly.

Table 6
Tower stay-cable topology.

Cable	Lower end			Upper end			Length[a]
	X (m)	Y (m)	Z (m)	X (m)	Y (m)	Z (m)	(m)
CB EAST 05	563.34	−248.08	56.96	487.49	−185.66	146.70	133.06
CB EAST 09	628.65	−294.29	55.22	488.74	−183.89	166.70	210.22
CB EAST 12	677.63	−328.94	53.80	489.68	−182.56	181.60	270.34
CB EAST 15	726.60	−363.60	52.27	490.46	−181.46	196.60	331.32
CB EAST 18	775.58	−398.25	50.64	491.15	−180.47	211.60	392.73
CB WEST 05	579.51	−225.23	56.96	495.40	−174.47	146.70	133.06
CB WEST 09	644.82	−271.43	55.22	494.15	−176.24	166.70	210.22
CB WEST 12	693.80	−306.08	53.80	493.21	−177.57	181.60	270.34
CB WEST 15	742.78	−340.74	52.27	492.43	−178.67	196.60	331.32
CB WEST 18	791.76	−375.39	50.64	491.73	−179.66	211.60	392.73

[a]Based on idealized geometry and does not reflect pre-tension of stay-cables.

Table 7

Measured stay-cable mass and stiffness properties for the entire length of each cable and pre-tension values in calm water conditions for each configuration. Values are averages for each cable set and F0 is the load level before the springs start to elongate.

| Cable set | Mass[a] (tonne/m) | Stiffness (kN/m) | Pre-tension (kN) | | | F0[a] (kN) |
			Configuration A	Configuration B	Configuration C	
CB 05	0.219	55260	13526	13390	13425	3490
CB 09	0.219	28960	12438	11727	11762	4339
CB 12	0.219	20883	12296	12172	12309	2908
CB 15	0.219	15957	14346	14547	14437	2582
CB 18	0.219	11131	12763	13433	12851	3054

[a] Estimated values.

Table 8

Estimated total stiffness properties of clamps and bridge girder following local bridge girder coordinate system. Here the Girder-Cables clamp values are the same as for the bridge girder without clamps.

Type	Location	Length (m)	EA_{zz} (kN)	EI_{xx} (kN m²)	EI_{yy} (kN m²)	GJ_{zz} (kN m²)
Girder-Cables-Girder	Sec-1 and Sec-3	6.20	3.137×10^{10}	9.898×10^{10}	1.413×10^{10}	1.617×10^{10}
Girder-Cables	Sec-2, Sec-4 and Sec-5	3.72	9.775×10^{9}	2.070×10^{10}	6.950×10^{8}	8.386×10^{8}
Girder-Column	Sec-6 to Sec-15	6.20	3.137×10^{10}	9.898×10^{10}	1.413×10^{10}	1.617×10^{10}

configurations in the Ocean Basin and the initial force F0 needed before the springs start to elongate. The measured axial stiffness is given as the total stiffness of the entire stay-cable assembly and includes contributions from the axial spring at the upper end, the steel rod constituting most of the cable length, the force transducer, the transverse aluminium girder and the clamped connection to the bridge girder.

2.7. Model connectivity

A rigid connectivity between the bridge elements is achieved using rigid, clamped connections between the cables, bridge girder elements, columns and pontoons. These clamped connections are custom designed for each specific connection along the bridge to facilitate the correct relative element-to-element positions along the bridge girder due to the changing azimuth and declination angles of the local bridge girder coordinate system, as well as stay-cable orientations. The only non-unique connection is the one between pontoons and their respective columns, cf. Figs. 4(c) and 6(c). An illustration of the location of the various clamped connection types can be seen in Fig. 2. When designing the clamped connections between the various bridge elements, focus is placed on correct geometrical connectivity as well as high rigidity and low mass properties. To keep the mass low, aluminium is used as the main material. Pictures of the three main types of claps used are shown in Fig. 6. All connections are bolted together and specifically the connections between the bridge girder components shown in Figs. 6(a) and 6(c) are fabricated with a small gap between the upper and lower plates in order to utilize maximum surface friction effects.

All connections are designed to work as rigid, clamped connections between the various bridge elements and can be considered as such. Due to the increased outer dimensions, the effective cross-sectional stiffness properties are significantly larger than the values listed for the bridge girder cross-section in Table 2. The total cross-sectional stiffness properties of the various clamped connections and the bridge girder are estimated based on their outer dimensions and listed in Table 8. The Girder-Cables clamp is assumed to have a low contribution to the stiffness properties and values for the bridge girder is instead used.

All clamped connections increase the mass along the bridge girder and at the top of the pontoons. The reader is referred to Appendix A for detailed information on the mass- and inertia properties of the distributed ballast, clamped connections and instrumentation. For each pontoon there is a stiff assembly to the bottom of the connecting pontoon column. The mass of this assembly is 50.7 tonne and is located at the geometric centre of the pontoons at 3.118 m above the SWL. This point mass is <u>not</u> included in the pontoon mass and gyration radii otherwise listed in Table 5.

2.8. Model boundary conditions

Specified boundary conditions are installed at the two bridge girder ends, i.e. at Sec-0 for the cable-stayed bridge section and at Sec-16 for the floating bridge section. Furthermore, the ten stay-cables are fixed in all translational DOFs at the upper ends and otherwise free to rotate. Table 9 lists the boundary conditions for the bridge girder and the stay-cables.

The stay-cable boundary conditions are modelled using eye bolts at the upper end and by connecting to the shear force transducer at the lower end with an adjustable nut, allowing for rotations at each end of the stay-cable.

The bridge girder boundary conditions are designed to be either fully fixed or free, except for axial springs at Sec-0 and Sec-16, compensating for the larger axial stiffness of the bridge girder cross-section. Numerical studies showed that axial rigid body modes could be exited by the incoming waves and so it was decided to lock the axial spring at Sec-0 and only use the axial spring at Sec-16. An illustration of the bridge girder boundary condition structure at Sec-16 is shown in Fig. 7(a). The structure consists of a universal joint allowing for free rotation around the local girder z- and x-axes, while being fixed around the local y-axis. The fixed boundary conditions have been verified to be stiff enough to act as fixed DOFs for all practical purposes. The axial stiffness of the spring was checked by applying known forces in the axial direction and measuring the corresponding displacement for each load level. The resulting axial stiffness property was found to be slightly non-linear. A second-order polynomial was fitted to the measured values, see Eq. (1), to describe the non-linear behaviour. The polynomial units are Newton for the axial force F and metres for the axial displacement x in full scale. It can be argued whether the transverse DOF at Sec-16 should be modelled as flexible instead of fixed in order to increase similarity in the modal response between the truncated model and the full bridge model. In the present study the choice is fallen on the fixed solution as focus is on validation of numerical tools with respect to the hydrodynamic loads. From that perspective, it is imperative to not introduce more uncertainties than necessary. Furthermore, numerical comparisons between the truncated and full bridge prior to the model tests, have shown that the bridge girder strong axis bending moments related to horizontal motion of the bridge are dominated by wind loads. The same investigation showed that the bridge girder weak axis bending moments (known to be dominated by wave loads) are not sensitive to the boundary condition at Sec-16.

$$F(x) = 10^8 \cdot x \cdot \left(2.067 + 1.932 \cdot |x| \right), \qquad \text{for} \qquad |x| \leq 0.155 \text{ m} \qquad (1)$$
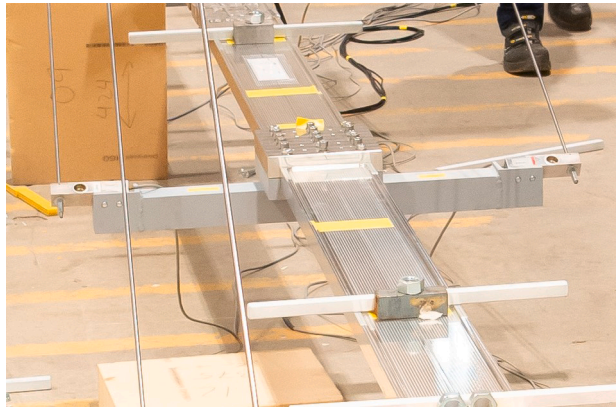
(a) Connection at Sec-3 between bridge girder elements and cables.

(b) Connection at Sec-4 between bridge girder and cables only.

(c) Column connection at Sec-8.

Fig. 6. Photos taken of representative clamped model connections during assembly of floating bridge model. Note that the connection depicted in (b) does not include a clamped connection between bridge girder elements as in (a).

Table 9
Boundary conditions given in local bridge girder and stay-cable coordinate systems.

Location	x (kN/m)	y (kN/m)	z (kN/m)	r_x (kN m/deg)	r_y (kN m/deg)	r_z (kN m/deg)
Girder Sec-0	Fixed	Fixed	$4.714 \times 10^{7\,a}$	$1.652 \times 10^{8\,a}$	$4.130 \times 10^{7\,a}$	Fixed
Girder Sec-16	Fixed	Fixed	cf. Eq. (1)	Free	$3.304 \times 10^{6\,a}$	Free
Cable upper ends	Fixed	Fixed	Fixed	Free	Free	Free
Cable lower ends	–	–	–	Free	Free	Free

[a]Stiffness equivalent to a fixed DOF for all practical purposes.

The bridge girder boundary condition at Sec-0 was build on a fixed steel frame, but instead of a universal joint on top, the bridge girder was firmly bolted to the centre steel box as shown in Fig. 7(b), resulting in a boundary condition that is, for all practical purposes, fixed in all DOFs. Note that although the bridge girder at Sec-0 is fixed to a similar axial spring structure as in Sec-16, the axial spring was locked during tests, resulting in a very stiff axial DOF.

3. Instrumentation and data acquisition

Standard sampling rate for the data acquisition system is 200 Hz (model scale), while the optical-electronic motion measurement system (MoCap) has a sampling rate of 50 Hz (model scale). All data is synchronized and re-sampled to 200 Hz (model scale). All sensors and gauges were calibrated prior to the model tests. Due to space considerations the full list of instrumentation used during the model tests is not given. Instead, a shorter list with only the most relevant measurements are given:

- Six DOF motion measurements of each pontoon.
- Three DOF translational motion measurements at 13 locations along the bridge girder.
- Wave elevation measured at the centre of the Ocean Basin.
- Six DOF measurement of loads acting at the cable-stayed bridge girder end.
- Six DOF measurement of loads acting at the floating bridge girder end.
- Five DOF measurement of loads at 10 locations along the bridge girder.
- Axial forces at the bottom of the stay-cables.

3.1. Motions of the pontoons and bridge girder

The global motion responses of the pontoons are measured by the MoCap system, which requires a minimum of three light-emitting diodes placed on each pontoon to measure the motion responses in six DOFs. Cameras located onshore along the basin are used to determine the position of the pontoons. Translational motions of the pontoons are
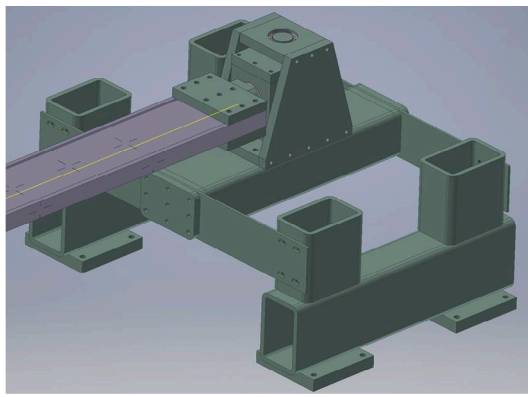
(a) Sketch of as-build girder boundary condition at Sec-16.
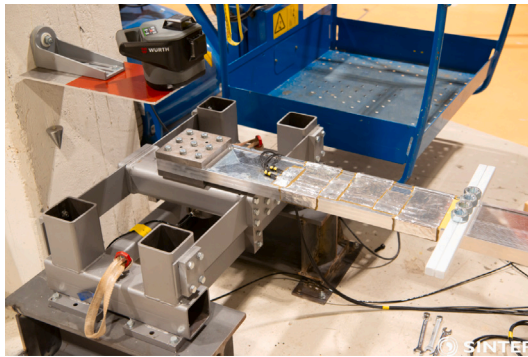
(b) As-build girder boundary condition at Sec-0.

(c) As-build stay-cable boundary conditions at tower end.

Fig. 7. Sketch and photos taken of boundary conditions during assembly of the floating bridge.

termed XPOS, YPOS and ZPOS for motion along the x-, y- and z-axis, respectively, in the local pontoon coordinate systems. The corresponding rotations around said axes are referred to as PITCH, ROLL and YAW. Note that all motions from the model tests are reported relative to the calm water position. The only exception is YAW, which is reported relative to the unique azimuth angle for each pontoon around the global Z-axis, listed in Table 3. Three DOF translational motions at 13 locations along the bridge girder were measured by using a single diode at each location. The reported motions along the bridge girder consist of pure translations along the axes in the local bridge girder coordinate system. The locations of the 13 diodes along the bridge girder are summarized in Table 10 for the three different configurations. These values are presented in the global coordinate system and also indicated in Fig. 2(b).

3.2. Forces and moments acting on the bridge girder

Shear forces and bending- and torsional moments are measured in the bridge girder using strain gauges. These measurements are taken at the two ends of the bridge girder, at the midspan between pontoons and at the middle of the main span. The locations at which the forces and moments are measured are summarized in Table 11 and illustrated in Fig. 2(b). Note that the force measurements were 6 DOF at the bridge ends, while 5 DOF measurements were recorded elsewhere.

The axial force is measured using a force transducer at Sec-0 and a displacement sensor at Sec-16. From the measure axial translation, the axial force is calculated from the known stiffness properties of the axial spring. This spring was calibrated prior to the model tests and the displacement-to-force relationship of the axial spring is discussed in Section 2.8.

Table 10

Location of reference points for the MoCap measurements along the bridge girder roadline relative to Sec-0. The actual diodes are positioned at a slight vertical distance from the bridge girder neutral axis. This distance x refers to distance along the direction of the x-axis in the local bridge girder coordinate system. The diodes H1, H2, H3 and H4 are located at x values of 4.898 m, 4.495 m, 4.774 m and 4.619 m, respectively, while all the diodes starting with B are located at $x = -5.115$ m and at an offset $z = 7.13$ m from the actual midspan. The X, Y and Z notations used in the measurement notation refer to the translational motion along the local bridge girder coordinate system axes.

Location ID	Roadline (m)	Measurements (m)	Position close to
H1	182.20	HX1, HY1, HZ1	Sec-2
H2	243.70	HX2, HY2, HZ2	Sec-3
H3	302.30	HX3, HY3, HZ3	Sec-4
H4	368.40	HX4, HY4, HZ4	Sec-5
B1	449.50	BX1 2, BY1 2, BZ1 2	Sec-6 and Sec-7 midspan
B2	574.50	BX2 3, BY2 3, BZ2 3	Sec-7 and Sec-8 midspan
B3	699.50	BX3 4, BY3 4, BZ3 4	Sec-8 and Sec-9 midspan
B4	824.50	BX4 5, BY4 5, BZ4 5	Sec-9 and Sec-10 midspan
B5	949.50	BX5 6, BY5 6, BZ5 6	Sec-10 and Sec-11 midspan
B6	1074.50	BX6 7, BY6 7, BZ6 7	Sec-11 and Sec-12 midspan
B7	1199.50	BX7 8, BY7 8, BZ7 8	Sec-12 and Sec-13 midspan
B8	1324.50	BX8 9, BY8 9, BZ8 9	Sec-13 and Sec-14 midspan
B9	1449.50	BX9 10, BY9 10, BZ9 10	Sec-14 and Sec-15 midspan

3.3. Axial forces in the stay-cables

The reported axial force measurements in the stay-cables contain both the static pre-tension and the dynamic axial force for each stay-cable. A photo of the force transducers used to measure the axial forces in each cable is presented in Fig. 5(b). The pre-tension in each stay-cable is tuned for each configuration as the final stage in the installation process using the nuts at the end of the stay-cables. After the final

Table 11
Location of measurement positions for forces (FX,FY,FZ) and moments (MX,MY,MZ) in the bridge girder. The X, Y and Z notations used in the measurement notation refer to the local axes of the bridge girder coordinate system. The forces and moments are acting along and around said axes, respectively. Position is given as distance along the roadline relative to Sec-0.

Location ID	Roadline (m)	Measurements (N) or (N m)	Description
END1	0.00	FX, FY, FZ, MX, MY, MZ	Sec-0
HB2	192.39	FX, FY, MX, MY, MZ	Sec-0 and Sec-6 midspan
FB1	442.50	FX, FY, MX, MY, MZ	Sec-6 and Sec-7 midspan
FB2	567.50	FX, FY, MX, MY, MZ	Sec-7 and Sec-8 midspan
FB3	692.50	FX, FY, MX, MY, MZ	Sec-8 and Sec-9 midspan
FB4	817.50	FX, FY, MX, MY, MZ	Sec-9 and Sec-10 midspan
FB5	942.50	FX, FY, MX, MY, MZ	Sec-10 and Sec-11 midspan
FB6	1067.50	FX, FY, MX, MY, MZ	Sec-11 and Sec-12 midspan
FB7	1192.50	FX, FY, MX, MY, MZ	Sec-12 and Sec-13 midspan
FB8	1317.50	FX, FY, MX, MY, MZ	Sec-13 and Sec-14 midspan
FB9	1442.50	FX, FY, MX, MY, MZ	Sec-14 and Sec-15 midspan
END2	1630.00	FX, FY, FZ, MX, MY, MZ	Sec-16

Table 12
Location of the reference wave probe and current metre during wave calibration in the global coordinate system, prior to the performed tests.

Configuration	X (m)	Y (m)
Configuration A	1210.75	−628.16
Configuration B	1221.56	−529.22
Configuration C	570.25	−809.12

adjustments the axial forces are measured and stored as static pre-tension values and the measurements are afterwards set to zero. The dynamic axial forces are measured by periodically zeroing of the axial force measurements before each test in order to avoid drift. In the post-processing phase the measured pre-tensions are then added to the dynamic axial force recordings.

3.4. Wave elevation and current

The reference wave elevation and the current velocity are measured at the centre of the Ocean Basin during the wave- and current calibration tests without the floating bridge. The location of the reference wave probe and the current metre in the global coordinate system is provided in Table 12.

3.5. Accuracy of bridge geometry and measurements

During installation of the bridge in the Ocean Basin, the static position of the bridge was checked in calm water conditions without current. The measured position of the pontoons deviate slightly from the idealized geometry in Table 3, although the radial distance in the global XY-plane is within 0.7 m from the idealized geometry listed in Table 1 for all three configurations, and the pontoon azimuth is within 0.3°. The waterline of the ten pontoons was carefully checked for the final calm water position for each configuration in the Ocean Basin and found well within the acceptable limits. This check confirmed that the total mass and the distribution of the mass along the bridge were acceptable.

The accuracy of the sensors used in the model tests have been assessed from calibration tests prior to the experiments. The accuracy of the measured parameters is given in Table 13. The accuracies are generally better than the tabulated values.

4. Model test program

The model test program consists of three phases: (i) wave and current calibration, (ii) system documentation tests and (iii) model testing. The first phase includes calibration of the waves generated

Table 13
Accuracy levels in model scale of the sensors/gauges used in the present model tests.

Sensor/gauge	Unit	Accuracy
Wave probe	mm	< ±0.20
Shear forces	N	< ±0.50
Moments	N m	< ±0.50
Axial forces at bridge ends	N	< ±0.20
Axial forces in cables	N	< ±0.20
Translational motion (MoCap)	mm	< ±0.20
Angular motion (MoCap)	deg	< ±0.05

Table 14
Overview of documentation tests for configuration A. The test ID letters ST/SD indicate if it is a static or decay test type, H/V/R indicate horizontal/vertical/roll test types, and the first and second number reflect position and load level, respectively. For all tests except the roll tests, the position is given along the bridge girder z-axis relative to Sec-0. For roll tests, the position numbers 1, 2 and 3 indicate loads applied at Pontoon-1, Pontoon-6 and Pontoon-10, respectively, with the corresponding position values along the pontoon y-axes. Positive force direction follow that of the local coordinate system axes.

Test ID	Position (m)	Load level # (kN) 1	2	3	4	5
ST-H1#	190.00	2995.56	5991.12	8986.68	11982.24	–
ST-H2#	694.36	1497.78	2995.56	4493.34	5991.12	7488.90
ST-H3#	1323.70	−2995.56	−5991.12	−8986.68	–	–
ST-V1#	190.00	5991.12	8986.68	11982.24	–	–
ST-V2#	694.36	5991.12	8986.68	11982.24	–	–
ST-V3#	1323.70	5991.12	8986.68	11982.24	–	–
ST-R1#	24.00	−5991.12	−8986.68	−11982.24	–	–
ST-R2#	24.00	−5991.12	−8986.68	−11982.24	–	–
ST-R3#	24.00	−5991.12	−8986.68	−11982.24	–	–
SD-H1#	376.28	4115.90	7614.71	13054.65	–	–

in the basin such that they meet the specified wave conditions and calibration of the current generated in the basin. The second phase involves documentation tests of the static and dynamic behaviour of the model, including pure current tests. The third phase involves wave testing, both with and without current. Due to space considerations, focus is put on the performed documentation tests in order to verify that the as-build model behaves as expected.

4.1. Documentation tests

The static and dynamic documentation tests in the Ocean Basin were carried out by various pull-out tests, cf. Table 14. The shown responses are the difference between the structure at rest before and after the force is applied. In order to avoid being in contact with the model or disturbing the water, the tests were performed from a movable platform.

Each of the vertical pull-out tests are performed by hanging an object with a mass, corresponding to the load level in Table 14, at the specified position via strings. Horizontal pull-out tests are performed in the same manner using a pulley to convert the gravitational force from the hanging mass to a horizontal force. Each of the roll tests are performed by positioning a mass at a given position on one of the pontoons. A resulting vertical force and pitching moment is generated at the given pontoon.

4.2. Current tests

The current was calibrated at the centre of the Ocean Basin prior to the model tests. Two current velocities were specified: 1.00 m/s and 1.50 m/s. These refer to the 1-year and 10-year current velocities at a depth of 1.5 m, based on Statens vegvesen (2018). The former was achieved within the acceptance criteria, whereas the latter was measured to be 1.44 m/s (4 % lower than specified) due to the relative large depth in the Ocean Basin. The current calibration tests were conducted for 2100 s (model scale).
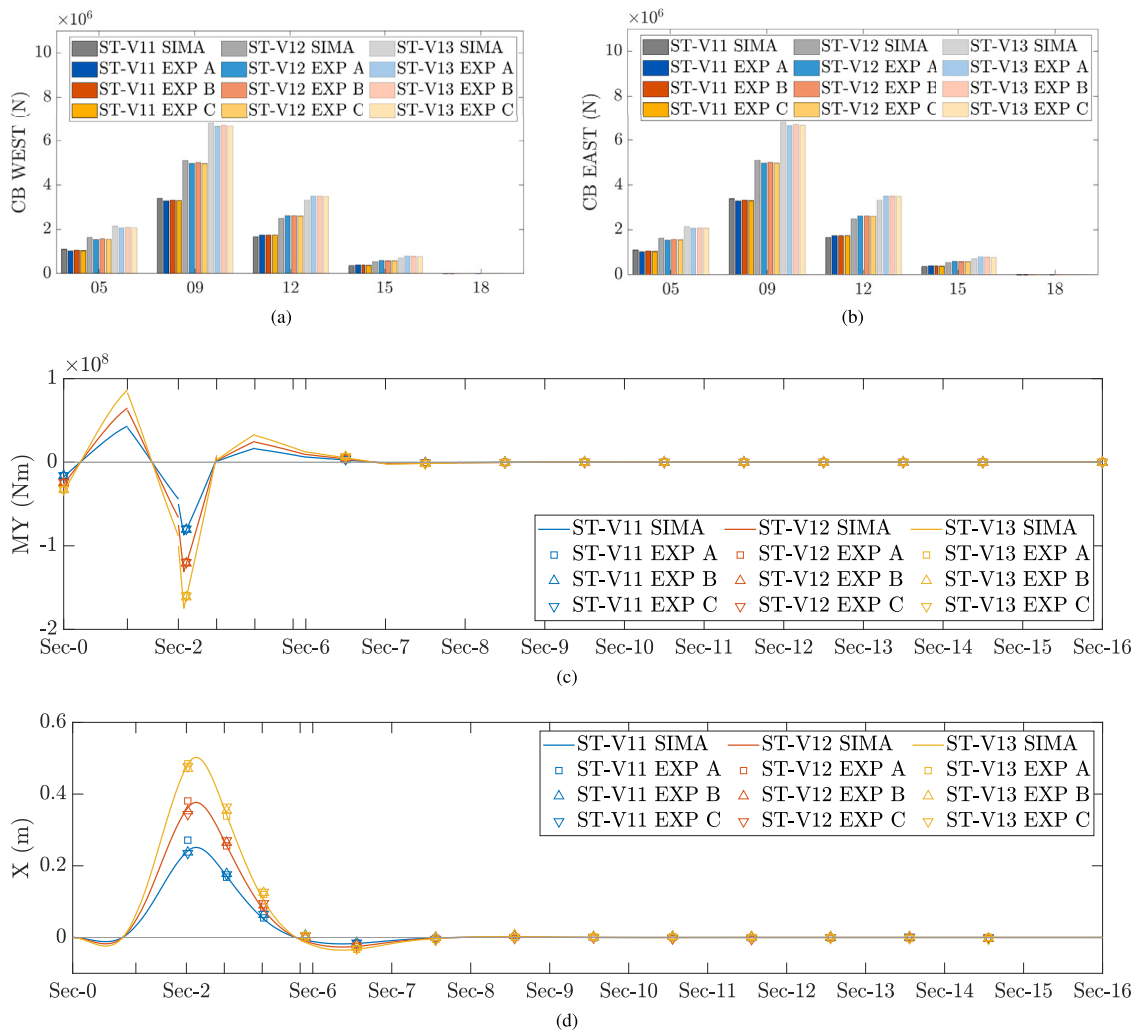
Fig. 8. Comparison of static vertical pull out test responses between model tests and the numerical model in SIMA. The comparison is based on a representative selection for all three configurations. (a) Tower stay-cable tension in West side cables, (b) Tower stay-cable tension in East side cables, (c) Girder weak axis bending moment, (d) Vertical motion in bridge girder local coordinate system.

4.3. Regular wave tests

Regular waves were calibrated for specified wave heights between 0.20 m and 3.00 m (most of which were close to 1.00 m) and wave periods ranging from 4.00 s to 18.00 s with intervals of 0.20 s and 0.50 s below and above 11.00 s, respectively. Besides this range, two extra regular wave periods (13.80 s and 14.20 s) were included in the test matrix.

4.4. Irregular wave tests

All irregular sea states were represented by the three-parameter JONSWAP spectrum according to DNV-RP-C205 (DNV, 2010, Section 3.5.5), with the significant wave height H_s, wave peak period T_p and peak enhancement factor γ. For short-crested, irregular waves, the directional distribution was generated based on the $D(\theta_0, \theta, n)$ function defined in DNV (2010, Section 3.5.8.4), which takes the arguments θ_0 as the main wave direction, θ as the wave direction component and n as the spreading exponent. 100 directional components were used in the generation of the short-crested waves. The duration of these tests were chosen as 3 h (+40 min) in full scale, as the model was assumed to need the extra 40 min to reach steady-state. The reader is referred to Appendix B for a full overview of the performed tests with waves.

5. Results and discussion

For each of the three configuration in the Ocean Basin, several documentation tests and wave tests (with or without current) were conducted. Due to space consideration, only a selection of the results from the documentation tests and pure current tests is presented in the present paper.

The model test responses were compared to a numerical model as part of the quality assurance of the model construction. This numerical model reflects the as-build, truncated, floating bridge and the structural parameters used in the numerical model were the same as the ones listed in the present paper. Only differences are the exclusion of the initial force F0 before elongation in the stay-cables starts and minor changes of the static load positions, which in the numerical model are located 1.60 m north of the exact midspan positions due to modelling consideration prior to the model tests. Note that the numerical estimates are only to be used as a reference, while the empirical results are considered the true response of the truncated bridge model.

5.1. Preliminary tests of the cable-stayed tower

Preliminary static tests of the cable-stayed bridge section by itself (excluding the clamp, column and pontoon at Sec-6 and the rest of the floating bridge section) were performed before the assembly in the
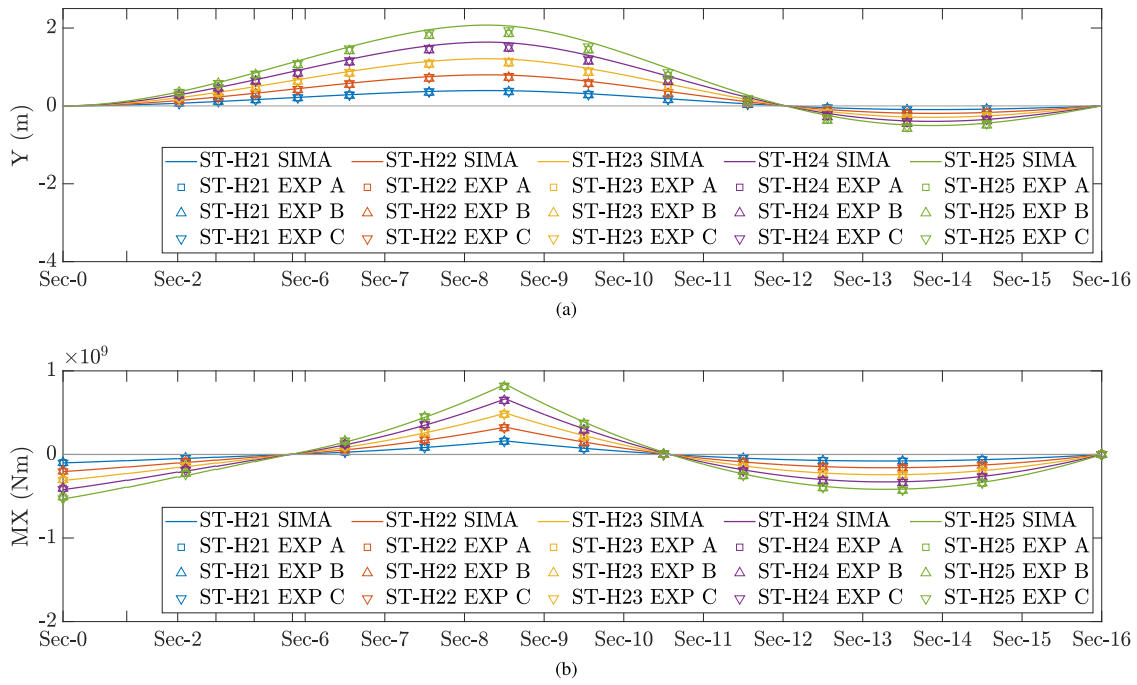
Fig. 9. Comparison of static horizontal pull out test responses between model tests and the numerical model in SIMA. The comparison is based on a representative selection for all three configurations. (a) Horizontal motion in the local bridge girder coordinate system, (b) Strong axis bending moment in the local bridge girder coordinate system.

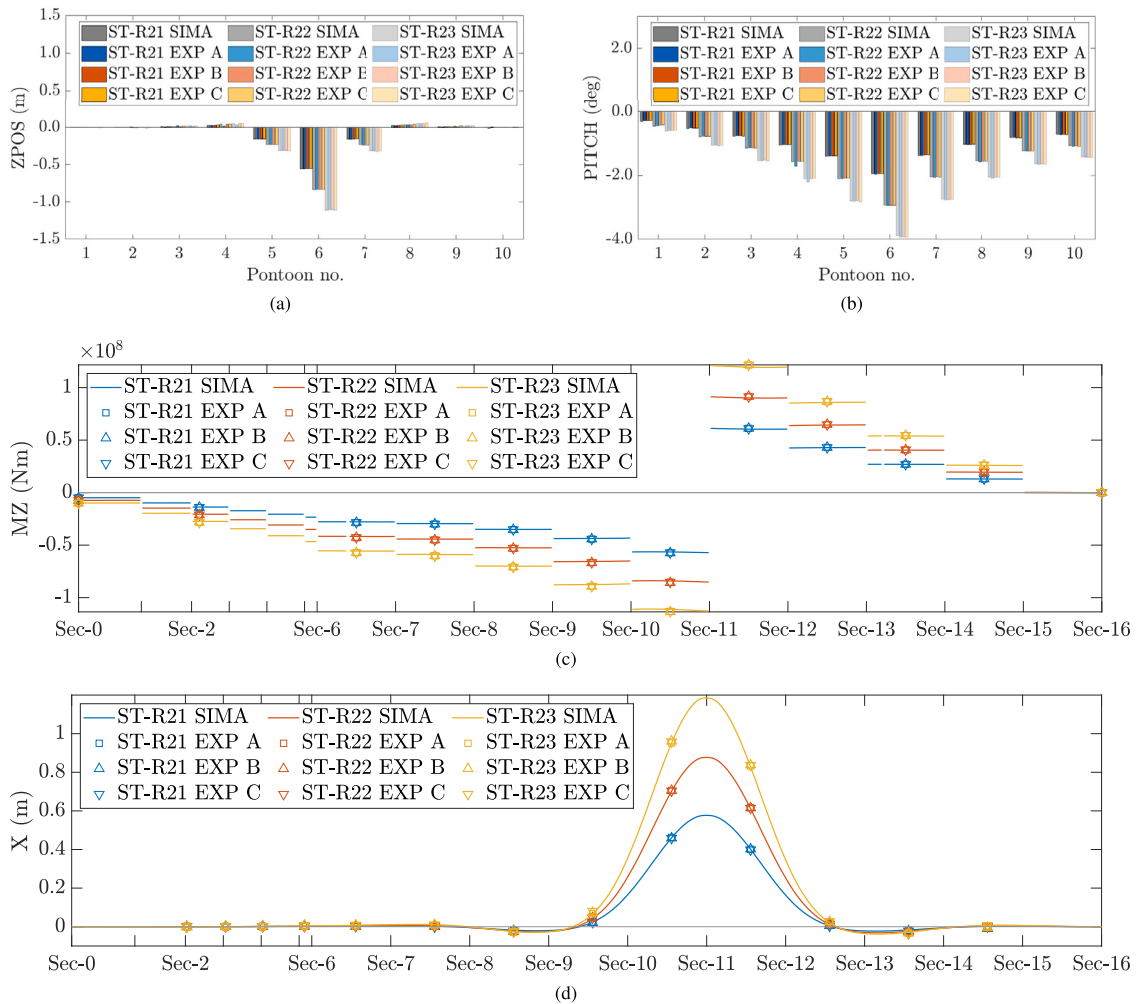**Fig. 10.** Comparison of combined static pull out test responses between model tests and the numerical model in SIMA. The comparison is based on a representative selection for all three configurations. (a) Pontoon vertical motion in the local coordinate system, (b) Pontoon pitch motion around the local *x* axis, (c) Girder torsional moment, (d) Vertical motion in bridge girder local coordinate system.
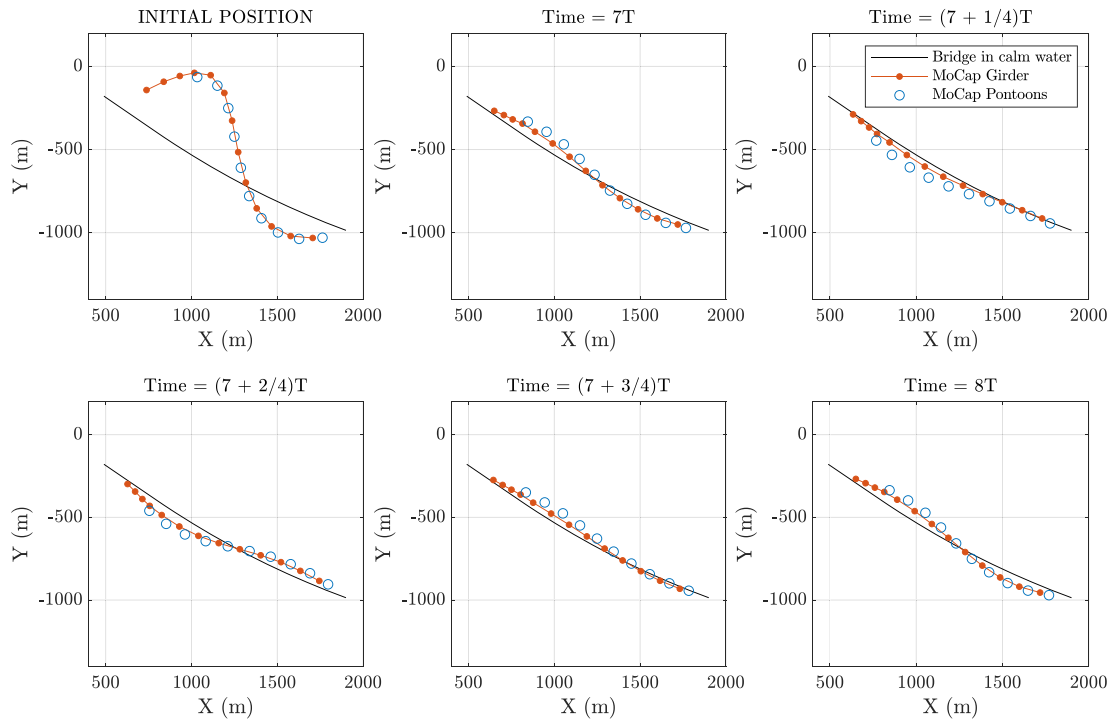
Fig. 11. Initial position and time instances of the *quasi-steady-state* oscillation with period *T* = 15.1 s for test SD-H13 after the first 7 oscillations. The relative positions are measured with the MoCap system and is scaled with a factor 150 for readability.
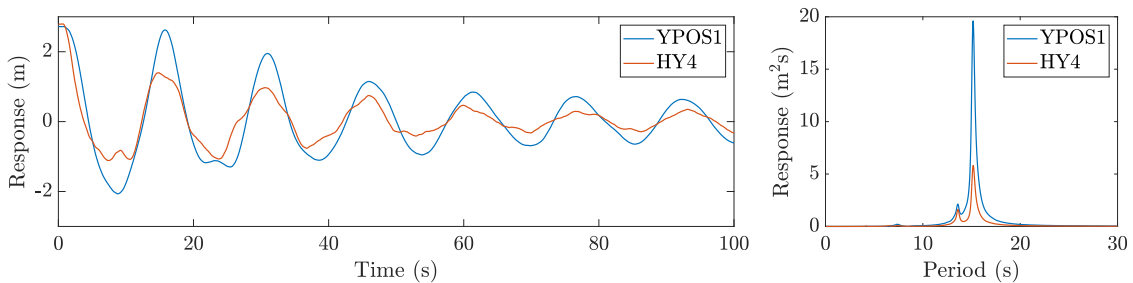

Fig. 12. Measured transverse response timeseries at H4 and Pontoon-1 for decay test SD-H13. The responses are measured along the local *y*-axes.

Ocean Basin. These tests confirmed that the bridge girder geometry and stay-cable pre-tension values were within the acceptable limits. Compared to numerical results, the deviations in the vertical position of the bridge girder were measured to be within 4 % of the bridge girder height reported in Xiang and Løken (2020) and the deviations in pre-tension values were between 2-10 %. Although the deviation in the static pre-tension is somewhat large, the effect of the increased non-linear stiffness contribution of the stay-cables was evaluated not to have a significant impact on the dynamic response of the floating bridge.

5.2. Static pull out test results for all three configurations

A relevant selection of responses are shown in Fig. 8 for the static vertical pull-out tests ST-V11, ST-V12 and ST-V13. These specific tests reflect the static response from vertical loads applied at the midspan between the tower and the first pontoon and illustrate best the inter-action of the bridge girder bending stiffness and the axial stiffness of the stay-cables. Looking at the numerical results, it is observed that the largest vertical deflection X in the local bridge girder coordinate system is located at the midspan where the load is applied. This is also reflected in the weak axis bending moment response MY in the local bridge girder coordinate system, where the largest negative moment coincides with this position along the arch length. The measured and

calculated cable axial forces also show largest values for CB 09 attached to Sec-2. The axial forces in cable sets CB 12 and CB 05 are similar in magnitude although the vertical deflection at Sec-3 is significantly larger than at Sec-1. One reason for this is the relatively larger axial stiffness in CB 05. Generally speaking all three response types compare well with the expected numerical calculations. However, there is a noteworthy difference in the vertical deflection measured close to Sec-2. With the complex geometry around the tower much effort was put on preliminary tests to properly estimate the total cable stiffness as a combination of contributions from all the structural parts involved, see Section 2.6. With these stiffness properties included in the numerical model, it is unlikely that the differences in the deflection at this location are due to erroneous modelling of the cable stiffness properties. Instead, the initial force F0 needed before the springs start to elongate is excluded in the numerical model, which might explain some of the observed differences. Another likely reason is the fact that the MoCap measurement system had difficulties measuring displacements around the tower for this specific load case. To apply the load at this location without disturbing the water, a moving platform was used. It is likely that the platform was blocking some of the cameras used in the MoCap system, disturbing the measurements in this particular case.

The static response related to the bridge girder strong axis bending stiffness is shown in Fig. 9 for the horizontal pull out tests ST-H21, ST-H22, ST-H23, ST-H24 and ST-H25. These are the horizontal deflection

Y and the strong axis bending moment MX in the local bridge girder coordinate system. Five different load levels are applied at the midspan between Sec-8 and Sec-9. Looking at the strong axis bending moment, it is clear that the applied loads introduce almost exactly the same moment response shape along the bridge girder. More importantly, both the measured and calculated moments are zero at Sec-16, confirming that the boundary condition is modelled correctly. Instead, small deviations is observed between the measured and calculated horizontal deflection which seem to increase with the load level. With the complex, curved geometry of the bridge, the horizontal and torsional response of the bridge is coupled, making it difficult to isolate the reasons for this behaviour. With the same behaviour for all measurement positions, the source of error related to the MoCap measurements is not a probable reason in this case. One reason could be that the structural coupling between the horizontal and torsional response introduces rotation of the bridge girder, which in turn influences the MoCap measurements because the diodes are located at positions elevated from the bridge girder centreline. Instead, the numerical model takes the relative deflection at the centreline and thereby does not capture this effect. Another reason could be minor differences in the position of the applied loads. It was found in preliminary numerical studies that changes to the load position as well as the axial spring stiffness at Sec-16 would change the position of the zero-deflection point close to Sec-12.

With a better understanding of the structural response when the floating bridge is undergoing vertical- and horizontal loads, the combined vertical- and torsional response can be considered. This is done by applying various eccentric vertical loads at Pontoon-6. Fig. 10 illustrates the combined torsional stiffness from the bridge girder and the hydrostatic pitch stiffness of the ten pontoons for the combined pull out tests ST-R21, ST-R22 and ST-R23. Looking first at the torsional moment MZ in the local bridge girder coordinate system, it is observed that the measured and calculated moments are almost identical. Again, the fact that the torsional moment at Sec-16 goes to zero confirms that the boundary condition is modelled correctly. Although the weak axis bending moment is not shown here, the measured values show the same conformity with the calculated response. With an understanding of the forces throughout the structure being almost identical, the vertical girder deflection X and the pontoon vertical position ZPOS in the global coordinate system, both illustrate the combined effect of the girder weak axis bending stiffness and the pontoon heave stiffness. From the observed and calculate values, these stiffness properties are captured well within the acceptable range for the three closest pontoons and four closest MoCap diodes. After that, the deflection values are too small to properly evaluate. This is due to the high stiffness ratio $K_g/K_p = 1.85$ between the pontoon heave stiffness $K_p = A_w \rho_w g$ and the bridge girder weak axis bending stiffness $K_g = 48 E I_{yy}/L^3$, where 100 usually is considered very soft supports and 0 is considered very stiff supports (MUL, 2017). The variables used in the previous notations are A_w for waterplane area, ρ_w for water density, g for the gravitational constant, L for the span length between each pontoon and $E I_{yy}$ refer to the weak axis bending stiffness of the bridge girder. The pontoon pitch motion describes the rotation around the local pontoon x-axis and reflects the combined torsional stiffness of the bridge girder and the pontoon pitch stiffness. It is observed that for all pontoons, except Pontoon-4, the measured pitch motion is in good agreement with the calculated responses. This confirms a good agreement in not only the pontoon stiffness properties and the bridge girder torsional stiffness, but also the combined contributions from the pontoon mass, centre of gravity and buoyancy. In this case, the largest pitch motion is within 5° making the assumption of linearity a valid method in estimating the contribution of these values. Instead, the larger deviations at Pontoon-4 are difficult to explain. For all the other similar test types, these deviations did not show up in the measurements and in fact all pontoons showed the same good agreement for all tests. Although it is possible that the MoCap cameras were blocked for this specific configuration, it is unlikely, since

the moving platform was positioned around Pontoon-6 at the time of the measurements. With all other similar measurements of Pontoon-4 showing good agreement, it is considered an outlier in this case.

Finally, it is noted that for all three configurations the bridge gives close to identical responses, which confirms a satisfying accuracy in the (re-)assembly of the model.

5.3. Free decay tests

Numerical studies showed that the first three structural modes of the bridge girder are dominated by horizontal motion in the local bridge girder yz-plane and rotation along the bridge girder z-axis. For the first mode, torsion of the bridge girder is predominately around the first five pontoons, while it is mostly around the last five pontoons in the second mode. The little vertical motion that was found for these modes was related to the bridge girder around the stay-cables. Decay tests were performed in the Ocean Basin for Configuration A in order to excite the first horizontal modes. One type of decay test was performed for this configuration with three load levels, cf. Table 14. The load is applied at the bridge girder close to Sec-6 and is orientated in the horizontal direction following the local bridge girder y-axis. The position and force direction were decided prior to the model tests based on numerical studies. The motion response of the decay test is captured in an animation of the X and Y positions in the global coordinate system, based the MoCap diode measurements along the bridge girder and at the pontoons. See the section on supplementary data (Appendix C) for a link to the animation available online. The initial position, as well as five snapshots of the animated position at various time instances of the *quasi-steady-state* motion after seven oscillations have passed, are shown in Fig. 11. The response has been amplified with a factor 150 in order to see the motion clearer along the bridge.

Looking at the initial position in Fig. 11, the pontoons and the bridge girder show the same initial shape. The slight deviation in the pontoon positions is mainly due to the resulting torsion of the bridge girder. When the floating bridge is let go, the bridge girder starts moving towards the other side while the pontoons lag behind due to the larger mass. The first 100 s after the structure is let go are dominated by the pontoon inertia which keeps the bridge girder from moving in a pure back and forth oscillation. This is illustrated by the bridge girder response HY4 and the first pontoon YPOS1 response in Fig. 12. Both positions are close to Sec-6.

After this initial phase the motion starts to oscillate in the pattern illustrated in Fig. 11, although the torsion of the bridge girder, and especially the inertia forces of the first 5 pontoons, continue to dominate the response. From the response spectra in Fig. 12 it is clear that the transverse motion of Pontoon-1 is dominated by the first mode, while the bridge girder motion at Sec-6 is more influenced by the second mode. This is in accordance with the initial understanding of the first two horizontal modes found numerically.

5.3.1. Natural periods

Damped natural periods for the first and second horizontal modes of the experimental model are found from the strong axis bending moment response spectra and listed in Table 15 together with estimated undamped natural periods from the numerical model. The experimental natural periods are based on weighted average of the three frequencies closest to the peaks for each of the first two horizontal modes. The numerical natural periods are found by solving the eigenvalue problem while accounting for the frequency-dependent added mass of the pontoons via a manual iterative solution procedure for each mode.

5.3.2. Estimated structural damping

Based on preliminary decay tests of only the cable-stayed bridge section (only containing model parts from Sec-0 to Sec-6 excluding pontoon, column and clamp at Sec-6) the structural damping coefficient ξ_{struc} was estimated to be in the range of $0.04\% \leq \xi_{\text{struc}} \leq 0.08\%$. Based on these findings, the dominant damping contributions are thought to be those related to the potential- and viscous damping of the pontoons.
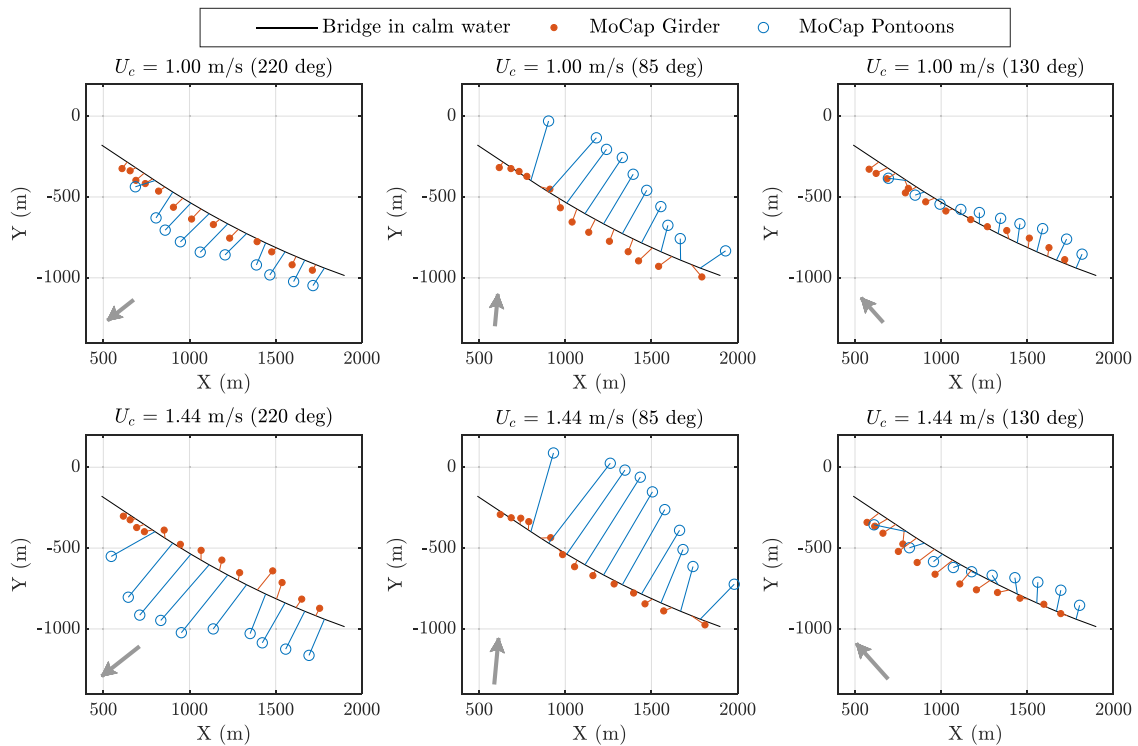
Fig. 13. Relative motion of pontoons and bridge girder diodes during pure current tests. The relative motion is scaled up with a factor 2500 for visibility and arrows indicate the current direction and the velocity.
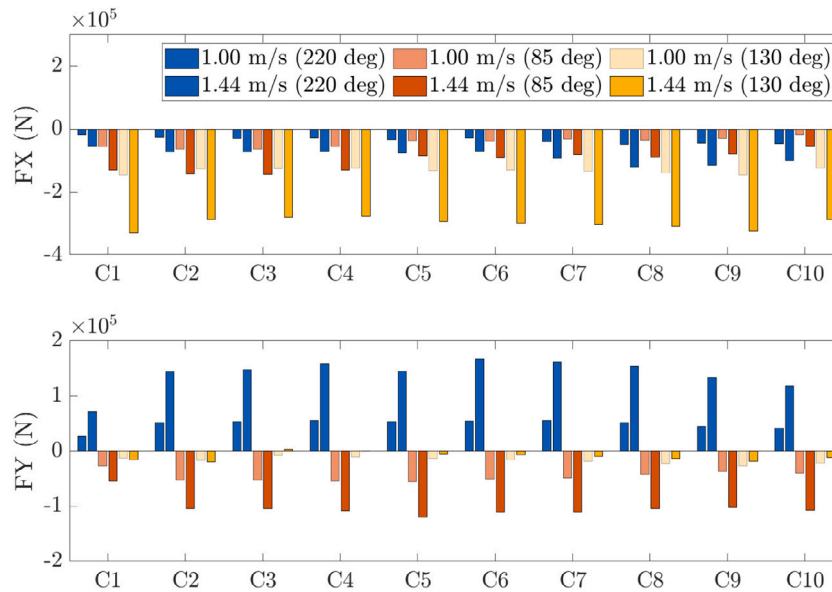
Fig. 14. Column shear forces during pure current tests. Notation follows the shared local pontoon and column coordinate system.

Table 15

Natural periods of floating bridge model. Measured damped natural periods are based on decay tests results. Numerically calculated natural periods are based on simulations in SIMA while accounting for frequency-dependent added mass of the pontoons and neglecting any damping.

Mode No.	Measured (s)	Calculated (s)
1	15.13	15.12
2	13.67	13.47

5.4. Current only tests

Pure current tests were performed for each configuration. These tests were conducted with two different current flow velocities, i.e. $U_c = 1.00$ m/s and $U_c = 1.44$ m/s. All tests were conducted for more than 3 h in full scale and results given in this section reflects time averaged values of each test relative to response values in calm water.

The relative motion of the bridge girder and pontoon diodes is illustrated in Fig. 13 with the relative motion scaled with a factor 2500 for visibility. For ease of reading the current direction and velocity is indicated with an arrow for each test. For the current velocity of 1.00 m/s in the direction going towards 220°, the motion responses

are observed to clearly follow the current direction. When the current speed is increased to 1.44 m/s, the pontoons clearly show an increase motion away from the initial position in the same direction as the current. However, the bridge girder does not follow this pattern and instead goes back to positions close to the calm-water position or to the opposite side of the girder. Looking at the motion responses for currents at a going towards direction of 85°, similar complex behaviour is observed when comparing tests with two different current velocities. In both cases, the pontoons move in the direction of the current with distances from the initial calm-water position correlating with the increase in current velocity. At the high current speed, the bridge girder does not move much, whereas at the low current speed the motion is generally opposite to the current direction. This complex behaviour observed for currents roughly perpendicular to the bridge is thought to be a combination of the double-curved geometry of the bridge girder, with an arch in the horizontal plane and a significant elevation of the bridge girder around the first four to five pontoons introducing both bending and torsion of the bridge girder.

By looking at the column shear forces presented in Fig. 14, it is observed that the current forces for each direction are roughly the same for all pontoons, with a few deviation due to pontoon azimuth angles and slight inhomogeneous current properties throughout the Ocean Basin. With the significant change in the bridge girder elevation along the length of the bridge, rotation of the bridge girder is more pronounced at positions in the vicinity of the first four to five pontoons. Another reason is the horizontal curvature of the girder, illustrated well by the motion responses for the 130° current tests. For this current direction, the column FX shear forces – an indirect measurement of the viscous drag forces from current flow around the pontoons – are roughly the same. The drag force on the first five upstream pontoons pushes the bridge towards the centre of the arc and as a consequence, the bridge girder rotates and at the opposite end the pontoons will move out and away from the centre of the horizontal arc.

6. Conclusion

An experimental study of a truncated section of the Bjørnafjord phase 5 K12 concept has been presented. The truncated section includes a simplified stay-cable tower and ten floating pontoons. The truncation points coincide with the tower column and the first moored pontoon of the full bridge. Here the boundary conditions in the bridge girder are simplified as fixed while allowing for free rotation around the vertical and longitudinal axes at the end with the otherwise moored pontoon. By reducing the initial length from 5530 m to 1630 m it was possible to build the model in scale 1:31 using Froude's scaling law.

The experimental model has a complex, double-curved geometry and consists of many different structural parts. A thorough description of the experimental model geometry and its stiffness- and mass properties was given for reproducibility, including relevant measurement positions and environmental conditions tested in the Ocean Basin. The many wave- and current directions tested were made possible by (re-)assembling the floating bridge in three different configurations in the Ocean Basin and the integrity of the as-build structure was verified for each configuration by comparing responses from static pull-out tests to numerical calculations. From these tests, the passive boundary conditions were verified, and the bridge responses were found to be well within the acceptable range, verifying the structural and hydrostatic stiffness properties. The largest deviations were found in responses associated with the intricate interaction between the tower stay-cable axial stiffness and the bridge girder bending and torsional stiffnesses, although these responses were also found to be within the acceptable range.

Pure current tests were performed with two current velocities corresponding to the 1-year and 10-year currents at the prototype location. Measured motion responses of the bridge girder and pontoons highlight the coupling between the horizontal motion and torsion of the bridge girder.

A decay test was performed to verify the dynamic properties of the experimental model. The initial motion showed a clear coupling between the transverse motion in the horizontal plane and rotation of the bridge girder due to the significant distance between the bridge girder centreline and the supporting pontoons. From the timeseries, the first two natural periods were found in compliance with the numerically estimated values.

CRediT authorship contribution statement

Thomas Viuff: Data curation, Formal analysis, Investigation, Validation, Visualization, Writing – original draft. **Senthuran Ravinthrakumar:** Funding acquisition, Investigation, Validation, Writing – review & editing. **Ole David Økland:** Investigation, Methodology, Project administration, Resources, Supervision, Validation, Writing – review & editing. **Ole Anton Grytå:** Resources, Supervision, Writing – review & editing. **Xu Xiang:** Conceptualization, Investigation, Methodology, Supervision, Validation, Writing – review & editing.

Declaration of competing interest

The authors declare that they have no known competing financial interests or personal relationships that could have appeared to influence the work reported in this paper.

Data availability

Data can be shared upon request and agreement with The Norwegian Public Roads Administration

Acknowledgements

Funding

Appendix A. Detailed mass information of instrumentation and clamps along the bridge girder

The mass- and inertia properties of the bridge girder are given in Table 2. Spread out along the bridge are various instrumentation and clamped connections to cables and pontoon columns. The mass- and inertia properties of these objects are given in Table A.16. These values do not include the actual bridge girder.

Appendix B. Full list of performed wave tests in the Ocean Basin

Table B.17 lists all irregular wave tests performed in the Ocean Basin. The waves are governed by the JONSWAP wave spectrum and the $\cos^s$ directional distribution function. The notation of the wave parameters are as follows: significant wave height (H_s), wave spectrum peak period (T_p), peak enhancement factor (γ) and spreading exponent (s). The main wave direction is indicated with θ_0 and the current velocity is indicated with the U_c notation.

Table A.16
Girder ballast along the roadline relative to the Sec-0 location. Mass and inertia values includes instrumentation and clamped connections.

Section	Length (m)	Mass (tonne)	CoG_x (m)	RoG_z (m)
Sec-0	0.000E+00	–	–	–
	2.099E+01	1.026E+02	−1.023E+00	4.210E+00
	3.333E+01	1.102E+02	−1.023E+00	4.210E+00
	5.000E+01	1.081E+02	−1.023E+00	4.210E+00
	6.667E+01	1.081E+02	−1.023E+00	4.210E+00
	8.333E+01	1.952E+01	−1.023E+00	5.660E−01
Sec-1	1.000E+02	3.335E+02	8.511E−01	5.658E+00
	1.160E+02	1.402E+01	−1.023E+00	5.660E−01
	1.320E+02	1.041E+02	−1.023E+00	4.210E+00
	1.480E+02	1.041E+02	−1.023E+00	4.210E+00
	1.640E+02	7.051E+01	−1.023E+00	2.869E+00
Sec-2	1.800E+02	2.022E+02	1.839E+00	7.673E+00
	1.885E+02	6.436E+01	−1.023E+00	2.869E+00
	2.100E+02	8.596E+01	−1.023E+00	4.210E+00
	2.250E+02	3.886E+00	0.000E+00	0.000E+00
Sec-3	2.400E+02	3.362E+02	8.511E−01	5.658E+00
	2.550E+02	4.004E+00	0.000E+00	0.000E+00
	2.700E+02	8.720E+01	−2.728E+00	1.519E+00
	2.850E+02	6.202E+01	−1.023E+00	2.869E+00
Sec-4	3.000E+02	2.005E+02	1.839E+00	7.673E+00
	3.150E+02	6.072E+01	−1.023E+00	2.869E+00
	3.300E+02	9.736E+01	−1.023E+00	4.210E+00
	3.450E+02	2.866E+01	−1.178E+00	1.354E+00
Sec-5	3.600E+02	1.989E+02	1.839E+00	7.673E+00
	3.700E+02	9.358E−01	0.000E+00	0.000E+00
Sec-6	3.800E+02	2.451E+02	0.000E+00	2.062E+00
	3.979E+02	6.527E+01	−2.728E+00	1.519E+00
	4.157E+02	1.160E+02	−3.503E+00	1.519E+00
	4.336E+02	1.148E+02	−1.178E+00	2.869E+00
	4.514E+02	1.172E+02	−1.178E+00	4.210E+00
	4.693E+02	1.161E+02	−1.023E+00	4.210E+00
	4.871E+02	8.622E+01	−1.798E+00	1.519E+00
Sec-7	5.050E+02	2.467E+02	0.000E+00	2.062E+00
	5.229E+02	8.523E+01	−1.023E+00	2.869E+00
	5.407E+02	1.172E+02	−3.348E+00	1.519E+00
	5.586E+02	1.172E+02	−1.023E+00	4.210E+00
	5.764E+02	1.172E+02	−1.023E+00	4.210E+00
	5.943E+02	1.161E+02	−1.023E+00	4.210E+00
	6.121E+02	8.011E+01	−2.418E+00	1.519E+00
Sec-8	6.300E+02	2.460E+02	0.000E+00	2.062E+00
	6.479E+02	8.002E+01	−1.023E+00	4.210E+00
	6.657E+02	1.166E+02	−2.883E+00	1.089E+00
	6.836E+02	1.169E+02	−1.178E+00	2.886E+00
	7.014E+02	1.162E+02	−1.178E+00	3.377E−01
	7.193E+02	1.161E+02	−1.023E+00	2.869E+00
	7.371E+02	7.095E+01	−2.418E+00	1.519E+00
Sec-9	7.550E+02	2.443E+02	0.000E+00	2.062E+00
	7.729E+02	7.031E+01	−1.023E+00	2.869E+00
	7.907E+02	1.174E+02	−2.728E+00	1.519E+00
	8.086E+02	1.172E+02	−1.178E+00	2.886E+00
	8.264E+02	1.172E+02	−1.023E+00	2.869E+00
	8.443E+02	1.161E+02	−1.023E+00	2.869E+00
	8.621E+02	6.484E+01	−2.418E+00	1.519E+00
Sec-10	8.800E+02	2.438E+02	0.000E+00	2.062E+00
	8.979E+02	6.420E+01	−1.178E+00	1.389E+00
	9.157E+02	1.180E+02	−2.728E+00	1.519E+00
	9.336E+02	1.158E+02	−1.178E+00	2.886E+00
	9.514E+02	1.172E+02	−1.023E+00	4.210E+00
	9.693E+02	1.161E+02	−1.023E+00	4.210E+00
	9.871E+02	6.179E+01	−1.798E+00	1.519E+00
Sec-11	1.005E+03	2.434E+02	0.000E+00	2.062E+00
	1.023E+03	6.115E+01	−1.178E+00	1.389E+00
	1.041E+03	1.156E+02	−1.798E+00	1.519E+00
	1.059E+03	1.157E+02	−1.178E+00	2.886E+00
	1.076E+03	1.171E+02	−1.178E+00	2.886E+00
	1.094E+03	1.159E+02	−1.023E+00	4.210E+00
	1.112E+03	5.554E+01	−2.418E+00	1.519E+00
Sec-12	1.130E+03	2.439E+02	0.000E+00	2.062E+00
	1.148E+03	5.490E+01	−1.023E+00	1.354E+00

(continued on next page)

Table A.16 (*continued*).

Section	Length (m)	Mass (tonne)	CoG_x (m)	RoG_z (m)
	1.166E+03	1.146E+02	−2.728E+00	1.519E+00
	1.184E+03	1.157E+02	−1.178E+00	2.886E+00
	1.201E+03	1.171E+02	−1.023E+00	4.210E+00
	1.219E+03	1.159E+02	−1.023E+00	4.210E+00
	1.237E+03	5.249E+01	−2.883E+00	1.519E+00
Sec-13	1.255E+03	2.429E+02	0.000E+00	2.062E+00
	1.273E+03	5.185E+01	−1.023E+00	1.354E+00
	1.291E+03	1.154E+02	−2.728E+00	1.519E+00
	1.309E+03	1.164E+02	−1.178E+00	2.886E+00
	1.326E+03	1.163E+02	−1.178E+00	2.886E+00
	1.344E+03	1.075E+02	−1.023E+00	4.210E+00
	1.362E+03	5.322E+01	−2.573E+00	1.519E+00
Sec-14	1.380E+03	2.444E+02	0.000E+00	2.062E+00
	1.398E+03	4.611E+01	−1.023E+00	1.354E+00
	1.416E+03	1.155E+02	−3.038E+00	1.519E+00
	1.434E+03	1.157E+02	−1.023E+00	4.210E+00
	1.451E+03	1.171E+02	−1.023E+00	4.210E+00
	1.469E+03	1.052E+02	−1.178E+00	2.886E+00
	1.487E+03	5.249E+01	−3.038E+00	1.519E+00
Sec-15	1.505E+03	2.427E+02	0.000E+00	2.062E+00
	1.523E+03	4.336E+01	−1.023E+00	2.869E+00
	1.541E+03	1.153E+02	−2.728E+00	1.519E+00
	1.559E+03	1.157E+02	−1.023E+00	4.210E+00
	1.576E+03	1.157E+02	−1.023E+00	4.210E+00
	1.594E+03	1.157E+02	−1.023E+00	4.210E+00
	1.612E+03	1.182E+02	−1.023E+00	4.210E+00
Sec-16	1.630E+03	–	–	–

Table B.17
Overview of specified irregular wave tests calibrated from wavemaker WM2 and WM3. Depending on the floating bridge configuration in the Ocean Basin, the wave will come from different main directions θ_0 in the global coordinate system. If no direction is listed under a configuration letter, then this wave is not used for that configuration.

Wave no.	Conf. and θ_0 (deg) A	B	C	WM (–)	H_s (m)	T_p (s)	U_c (m/s)	γ (–)	s (–)
84900[a]	220	85	130	WM2	1.00	3.5–20			
84910[a]	220	85	130	WM2	2.00	3.5–20			
84950[a]	220	85	130	WM2	1.00	3.5–20	1.00		
83312			130	WM2	1.50	5.00			2
82062	220	85		WM2	2.10	5.00			2
83361			130	WM2	1.50	5.20			2
82102	220	85		WM2	2.10	5.20			2
83402			130	WM2	1.50	5.50			2
82003	220	85		WM2	1.80	5.50			2
82162[b]	220	85		WM2	2.10	5.50			2
83461			130	WM2	1.50	5.90			2
82202	220	85		WM2	2.10	5.90			2
82355	220	85		WM2	2.70	5.90			2
83502			130	WM2	1.50	6.50			2
82252	220	85		WM2	2.10	6.50			2
82403	220	85		WM2	3.10	6.50			2
83552			130	WM2	1.50	7.00			2
82302	220	85		WM2	2.10	7.00			2
82452	220	85		WM2	3.10	7.00			2
83630			130	WM2	1.50	5.00	1.00		2
83652			130	WM2	1.50	5.20	1.00		2
82653	220	85		WM2	2.10	5.20	1.00		2
83703			130	WM2	1.50	5.50	1.00		2
82703	220	85		WM2	2.10	5.50	1.00		2
83752			130	WM2	1.50	5.90	1.00		2
82752	220	85		WM2	2.10	5.90	1.00		2
83802			130	WM2	1.50	6.50	1.00		2
82801	220	85		WM2	2.10	6.50	1.00		2
83851			130	WM2	1.50	7.00	1.00		2
82852	220	85		WM2	3.10	7.00	1.00		2
83053	220			WM2	2.10	5.20	1.50		2
83103	220			WM2	2.10	5.50	1.50		2
83153	220			WM2	2.10	5.90	1.50		2
83203	220			WM2	2.10	6.50	1.50		2

(continued on next page)

Table B.17 (continued).

Wave no.	Conf. and θ_0 (deg) A	B	C	WM (–)	H_s (m)	T_p (s)	U_c (m/s)	γ (–)	s (–)
83252	220			WM2	3.10	7.00	1.50	2	
82502	220	85		WM2	0.46	8.60		4	
82552	220	85		WM2	0.46	13.80		4	
82602	220	85		WM2	0.46	15.40		4	
82901	220			WM2	0.46	8.60	1.00	4	
82951	220			WM2	0.46	13.80	1.00	4	
83001	220			WM2	0.46	15.40	1.00	4	
85900[a]	310	175		WM3	1.00	3.5–20			
85910[a]	310	175		WM3	2.00	3.5–20			
85950[a]	310	175		WM3	1.00	3.5–20	1.00		
85002	310	175		WM3	1.50	5.00		2	
85052	310	175		WM3	1.50	5.20		2	
85102	310	175		WM3	1.50	5.50		2	
85152	310	175		WM3	1.50	5.90		2	
85201	310	175		WM3	1.50	6.50		2	
85252	310	175		WM3	1.50	7.00		2	
85301	310			WM3	1.50	5.00	1.00	2	
85351	310			WM3	1.50	5.50	1.00	2	
85401	310			WM3	1.50	6.50	1.00	2	
87401	310			WM3	1.50	5.20		2	4
87002			220	WM3	2.10	5.20		2	4
87451	310			WM3	1.50	5.50		2	4
87053			220	WM3	2.10	5.50		2	4
87511	310			WM3	1.50	5.90		2	4
87103			220	WM3	2.10	5.90		2	4
87561	310			WM3	2.30	6.50		2	4
87153			220	WM3	3.10	6.50		2	4
87600	310			WM3	2.30	7.00		2	4
87202			220	WM3	3.10	7.00		2	4
87252	310		220	WM3	0.46	8.60		4	10
87311	310		220	WM3	0.46	13.80		4	10
87352	310		220	WM3	0.46	15.40		4	10

[a]Whitenoise tests with T_p values indicating the spectrum limits.

[b]Repeated test with 10 different wave seeds.

Appendix C. Supplementary data

Supplementary material related to this article can be found online at https://doi.org/10.1016/j.apor.2023.103539. Supplementary material associated with this article can be found, in the online version, at (insert link to animation here).

References

Aarsnes, J.V., Stansberg, C.T., Reed, K., 1989. Modellforsøk Med Flytebru: Kontinuerlig Pontongbru. Report no. MT40 F89-0252, MARINTEK, Trondheim, Norway.

Aarsnes, J.V., Stansberg, C.T., Reed, K., 1990. Modellforsøk Med Flytebru: Enkelt Pontong. Report no. MT40 F89-0239, MARINTEK, Trondheim, Norway.

Abrahamsen, B.C., Stansberg, C.T., 2019. LFCS Review Report – Model Testing Model Testing of Large Structures in a Wave Basin. Report no. OC2018 A-073-WP5, SINTEF Ocean, Trondheim, Norway, http://hdl.handle.net/11250/2603349.

AMC, 2019. Preffered Solution, K12 - Main Report. SBJ-33-C5-AMC-90-RE-100, Statens vegvesen, Oslo, Norway, https://vegvesen.brage.unit.no/vegvesen-xmlui/handle/11250/2659842.

Baarholm, G.S., 2017. Model Tests for Bjørnafjorden Floating Bridge Concept. Report no. OC2017F-176, SINTEF Ocean, Trondheim, Norway.

Dai, J., Abrahamsen, B.C., Viuff, T., Leira, B.J., 2022. Effect of wave-current interaction on a long fjord-crossing floating pontoon bridge. Eng. Struct. (ISSN: 0141-0296) 266, 114549. http://dx.doi.org/10.1016/j.engstruct.2022.114549.

DNV, 2010. DNV-RP-C205 Environmental Conditions and Environmental Loads. Det Norske Veritas, Oslo, Norway.

Fergestad, D., Økland, O.D., Stefanakos, C., Stansberg, C.T., Croonenborghs, E., Eliassen, L., Eidnes, G., 2018. LFCS Review Report - Environmental Conditions Wind, Wave and Current in Coastal Areas. Report no. OC2018 F-073-WP1, SINTEF Ocean, Trondheim, Norway, http://hdl.handle.net/11250/2600265.

Fonseca, N., Bachynski, E.E., 2018. LFCS Review Report – Environmental Loads Methods for the Estimation of Loads on Large Floating Bridges. Report no. OC2018 A-073-WP2, SINTEF Ocean, Trondheim, Norway, http://hdl.handle.net/11250/2599735.

Holand, I., Sigbjörnsson, R., Langen, I., 1977. Dynamic analysis of a curved floating bridge. pp. P–5/77.

Kvåle, K.A., 2017. Dynamic Behaviour of Floating Bridges Exposed to Wave Excitation - a Numerical and Experimental Investigation (Ph.D. thesis). Norwegian University of Science and Technology, Trondheim, Norway, URL: http://hdl.handle.net/11250/2479175.

Leira, B., Kvittem, M.I., Alsos, H.S., Fylling, I.J., 2018. LFCS Review Report - Structure and Mooring Response. Report no. OC2018 A-073-WP3/WP4, SINTEF Ocean, Trondheim, Norway, https://hdl.handle.net/11250/2651594.

Løken, A.E., Oftedal, R.A., Aarsnes, J.V., 1990. Aspects of hydrodynamic loading and response in design of floating bridges. In: Second Symposium on Strait Crossings. Trondheim, Norway, pp. 479–486.

Moan, T., Eidem, M.E., 2020. Floating bridges and submerged tunnels in Norway - the history and future outlook. In: Wang, C.M., Lim, S.H., Tay, Z.Y. (Eds.), WCFS2019. Springer Singapore, Singapore, pp. 81–111. http://dx.doi.org/10.1007/978-981-13-8743-2_5.

MUL, 2017. SBJ-31-C3-MUL-22-RE-100 - Analysis and Design (Base Case). SBJ-31-C3-MUL-22-RE-100, rev 0, Statens vegvesen, Oslo, Norway, https://www.vegvesen.no/globalassets/vegprosjekter/utbygging/e39stordos/vedlegg/sbj-31-c3-mul-22-re-100-0-analysis-and-design-base-case.pdf.

Petersen, W., Øiseth, O., Lourens, E., 2019. Full-scale identification of the wave forces exerted on a floating bridge using inverse methods and directional wave spectrum estimation. Mech. Syst. Signal Process. 120, 708–726. http://dx.doi.org/10.1016/j.ymssp.2018.10.040.

Ravinthrakumar, S., Alsos, H., Økland, O.D., Lie, H., Xiang, X., Grytå, O.A., Kristiansen, T., 2023a. Forced motion of a floating bridge pontoon to evaluate the hydrodynamic damping properties. Appl. Ocean Res. (submitted for publication).

Rodrigues, J.M., Økland, O., Fonseca, N., Leira, B., Alsos, H.S., Abrahamsen, B.C., Aksnes, V., Lie, H., 2020. Design and verification of large Floating Coastal structures: Floating bridges for fjord crossings. URL: https://onepetro.org/ISOPEIOPEC/proceedings-pdf/ISOPE20/All-ISOPE20/ISOPE-I-20-1307/2249567/isope-i-20-1307.pdf. ISOPE-I-20-1307.

Rodrigues, J.M., Viuff, T., Økland, O.D., 2022. Model tests of a hydroelastic truncated floating bridge. Appl. Ocean Res. 125, 103247. http://dx.doi.org/10.1016/j.apor.2022.103247.

Shao, Y., Xiang, X., Liu, J., 2019. Numerical investigation of wave-frequency pontoon responses of a floating bridge based on model test results. http://dx.doi.org/10.1115/OMAE2019-96545.

SINTEF Ocean, 2021a. Large Floating Coastal structures (LFCS) project website. https://www.sintef.no/projectweb/lfcs/. Accessed: 2021-12-02.

SINTEF Ocean, 2021b. RIFLEX 4.20.2 Theory Manual. SINTEF Ocean, Trondheim, Norway.

SINTEF Ocean, 2021c. SIMO 4.20.2 Theory Manual. SINTEF Ocean, Trondheim, Norway.

Statens vegvesen, 1990. Sammenligning Mellom Modellforsøk og Beregninger av en Enkelt Pongtong og en Flytebru Med Separate Pongtonger. Report no. 89-3440, Vegdirektoratet, Høvik, Norway.

Statens vegvesen, 2018. MetOcean Design Basis. SBJ-01-C4-SVV-01-BA-001, Oslo, Norway, https://vegvesen.brage.unit.no/vegvesen-xmlui/handle/11250/2676915.

Viuff, T., 2020. Uncertainty Assessment of Wave- and Current-Induced Global Response of Floating Bridges - a Numerical Investigation (Ph.D. thesis). Norwegian University of Science and Technology, Trondheim, Norway, URL: https://hdl.handle.net/11250/2651104.

Viuff, T., Xiang, X., Leira, B.J., Øiseth, O., 2020a. Software-to-software comparison of end-anchored floating bridge global analysis. J. Bridge Eng. 25 (5), 04020022. http://dx.doi.org/10.1061/(ASCE)BE.1943-5592.0001545.

Viuff, T., Xiang, X., Øiseth, O., Leira, B.J., 2020b. Model uncertainty assessment for wave- and current-induced global response of a curved floating pontoon bridge. Appl. Ocean Res. 105, 102368. http://dx.doi.org/10.1016/j.apor.2020.102368.

Xiang, X., Løken, A., 2019. Hydroelastic analysis and validation of an end-anchored floating bridge under wave and current loads. In: Proceedings of the 38th International Conference on Offshore Mechanics and Arctic Engineering. pp. 1–9. http://dx.doi.org/10.1115/OMAE2019-95114.

Xiang, X., Løken, A., 2020. SBJ-32-C5-SVV-21-RE-003-0 Floating Bridge Hydrodynamic Model Tests Specification 3 – High Bridge Tests. Statens vegvesen report.

Xiang, X., Viuff, T., Leira, B., Øiseth, O., 2018. Impact of hydrodynamic interaction between pontoons on global responses of a long floating bridge under wind waves. http://dx.doi.org/10.1115/OMAE2018-78625.